**The Dissertation Committee for Qi Wang Certifies that this is the approved version of the following dissertation:**

# Deposition and Characterization of Thin Films for Applications in ULSI Fabrication

**Committee:**

**John Michael White, Supervisor**

**John G. Ekerdt**

**Yangming Sun**

**Gyeong S. Hwang**

**Kurt Junker**

# Deposition and Characterization of Thin Films for Applications in ULSI Fabrication

by

**Qi Wang, B. E., M. S.**

**Dissertation**

Presented to the Faculty of the Graduate School of

The University of Texas at Austin

in Partially Fulfillment

of the Requirements

for the Degree of

**Doctor of Philosophy**

The University of Texas at Austin

December 2004

# Dedication

To my parents and my wife

# Acknowledgments

I sincerely thank my advisor, Dr. John Michael White, for guiding me throughout the past five years with his patience, creativity, and profound wisdom. His instruction was not only limited to teaching me knowledge and technology, more importantly, he trained me to correctly analyze problems and discover the mechanisms behind experimental data, which benefited my entire professional career. I would also like to truly thank Dr. John G. Ekerdt for his great mentoring during the last two years of my Ph. D study. His broad knowledge, keen insight on key issues, and down-to-earth style with students made my study very fruitful and pleasurable. In addition, I extend my sincere gratitude to Dr. Yangming Sun. He taught me vital practical knowledge of the UHV system, thin film deposition, surface analysis and many other technologies. His invaluable advice and creative ideas helped me, in significant ways, to overcome countless difficulties throughout my entire graduate research. I was very fortunate to work with these three excellent mentors over the course of my program, and this work would not have been possible without their insightful guidance.

I would also like to thank all of my former and present colleagues in the White and Ekerdt groups for their great help during my graduate study at UT-Austin. I especially thank Wei Zhao, Bing Luo, Andrew Lemonds, Ward

Engbrecht, and Xiaoming Yan for offering great advice and helping me to resolve problems in varying aspects. My special thanks also go to Darren Gay, who worked with me as an undergraduate researcher throughout the last three years. His dedicated work was an important contribution to the accomplishments presented in the Chapter 4 and 5 of this dissertation.

I wish to express my deep appreciation for my proud parents Zhaozheng Wang and Xiaoying He for their continuous support and encouragement through all the years. To my beloved wife, Jinghua Pan, Thanks for all your loving care and for being behind me throughout all my endeavors. The encouragement from my entire family was and still is the motivation for me to overcome all difficulties on the road of my life. I dedicate this work to them.

# Deposition and Characterization of Thin Films for Applications in ULSI Fabrication

Publication No._____________

Qi Wang, Ph. D.

The University of Texas at Austin, 2004

Supervisor: John Michael White

When the ever-shrinking microelectronic device dimensions scale below 100 nm, introducing new material and processing technologies are necessitated to overcome forbidding obstacles in both front-end and back-end manufacturing processes. This dissertation first addresses the deposition of an $Al/Al_2O_3$ cermet film as a potential thermal resist material for electron beam projection lithography. The films were deposited by reactive sputter deposition and their transformations were investigated by irradiation with a single 1064 nm laser pulse in ambient air and $10^{-2}$ Torr vacuum. Irradiation in vacuum led to re-distribution of components within the first ~35 nm beneath the surface. Irradiation in air increased the

concentration of $Al_2O_3$ in the same region. Based on a model calculation, the observed transformations were interpreted as a result of local heating and, in air, as accompanying thermal oxidation. Second, a novel *in-situ* laser annealing system was developed for real time kinetic analysis on surface chemistry and thin film properties. A continuous wave $CO_2$ infrared laser was coupled to a surface analysis system equipped for x-ray photoelectron spectroscopy and ion scattering spectroscopy. The capability is illustrated by using real time XPS and ISS to measure the reduction kinetics of a thin copper oxide ($Cu_2O$) film.

Third, research efforts were focused on deposition and characterizations of a thin ruthenium film as a new copper diffusion barrier for ultra-large scale integrated circuit (ULSI) interconnect. A thermal chemical vapor deposition route using $Ru_3(CO)_{12}$ was developed to form pure, uniform, and smooth Ru films on Ta and low resistivity films on $SiO_2$. Measured using XPS and ISS and assuming smooth films, a 2.5 nm Ru film fully covers underlying Ta and $SiO_2$. Unlike Ta, the Ru film exhibits excellent wettability by Cu even when the Ru surface is contaminated with small amounts of oxygen. A 4 nm Ru film and a 2.9 nm Ru/0.6 nm Ta composite film are effective copper diffusion barriers under 60 minutes annealing at 623 K in $H_2(10\%)/N_2$ ambient.

# Table of Contents

# List of Tables

# List of Figures

# List of Illustrations

# Chapter 1

# Introduction

Modern integrated circuits (ICs) consist of hundreds of millions of devices which achieve complex functions. The demands for faster CPU speed, higher chip integration density, enhanced integrated circuit functionality, and reduced cost per function have been driving device scaling and increasing interconnect complexity [1]. As the microelectronic device dimensions keep shrinking, especially when the feature sizes scale below 100 nm, numerous challenges arise in both front-end and back-end manufacturing processes. Introducing new material and innovative deposition and characterization technologies are necessitated to overcome those forbidding obstacles. This dissertation reports my fundamental studies on deposition and characterization of thin films for the applications in future generations of front-end and back-end fabrication.

## 1.1 Development of new thermal resist for future electron beam projection lithography

Microlithography is one of the key fabrication technologies to manufacture semiconductor devices. This technology transfers images from a mask to the surface of a wafer in order to designate specific areas which form the devices required to make integrated circuits. Because current microlithography technology utilizes ultraviolet (UV) light to generate fine patterns on the wafer, it is typically called photolithography.

For a typical photolithography process, the wafer is first coated with a photosensitive polymeric material called "photoresist" by spin-coating. The resist-coated wafer is then contacted with a photo mask bearing fine patterns and exposed to UV light. After the exposure, the wafer is treated with a solution called "developer". According to the specific type of photoresist, the areas in the resist exposed to UV light are made either soluble or insoluble in the developer. After resist developing, the patterns have been transferred from the photomask to the photoresist. Next, this patterned photoresist is used as a mask for etching the exposed underlying layer. Finally, the photoresist is removed away from the patterned wafer surface by using stripping solution or oxygen plasma.

Motivated by scaling the IC feature size, photolithography used in the fabrication of high-performance IC has been constantly required to have much higher resolution capability. To satisfy this requirement, the wavelength of the UV light is shortened to 157 nm for the current technology node, and many other improvements have also been made in this technology. As a result, the minimum feature size has been reduced to the deep-submicron region, but it is now approaching the theoretical limit of resolution in photolithography [2-4].

Therefore, it is necessary to find a new lithography technology to pattern the IC for future technology nodes.

Electron beam projection lithography is one of the promising technologies for next generation lithography because of the extreme short wavelength of an electron beam. In order to implement this technology, significant changes in material and processes will likely be required. For example, it is worthwhile to pursue a new resist material since traditional resists for photolithography may not be applicable. Considering an electron beam can provide thermal energy to the exposed material, a potential thermal-sensitive resist, Al/$Al_2O_3$ cermet, was studied for the mechanism of its thermal transformation in this dissertation.

## 1.2 Development of new copper diffusion barriers for ULSI interconnect

### 1.2.1 Copper interconnect

Interconnect in IC devices are the wires that provide the power, the ground, inputs and outputs and timing signals to microelectronic devices. These layers of "wiring" are classified into local, intermediate and global levels. Local wiring is comprised of the first two levels of wiring above the transistors, which are followed by the intermediate (middle) and global (topmost) levels. Aluminum (Al) was traditionally used as the metal interconnect, and silicon dioxide ($SiO_2$) was the insulating dielectric which isolated neighboring Al wires.

The speed of an electrical signal in an IC is governed by two factors – the switching time of an individual transistor and the signal propagation time across interconnect [5]. The signal transmission in the interconnect is limited by a time delay, known as *RC* time delay, which is proportional to the product of the resistance (*R*) of the metal wire lines and the capacitance (*C*) due to the insulating dielectric layers. The total resistance of the conductor is a function of its physical dimensions (length, *L*, and thickness, *t),* and resistivity, ($\rho$). The capacitance is proportional to the dielectric constant ($\kappa$) of the dielectric and inversely proportional to the spacing between metal lines (*d*) [6]. The *RC* time delay, $\tau$, follows the relation: [7]

$$\tau = RC \propto \frac{\rho \kappa L^2}{td}$$

As $t$ and $d$ scale down, $\tau$ will increase. This RC delay was negligible when the feature size was larger than 1 μm. However, for sub-micron technology, the RC delay plays an increasing role in overall chip performance, as shown in Figure 1.1 [8]. For integrated circuits at the 250 nm node or below, the interconnect time delay is the limiting factor for microprocessor speed [9,10].

To facilitate further improvements, new materials are forced to introduce into chip production. These new materials should be used to reduce the RC delay

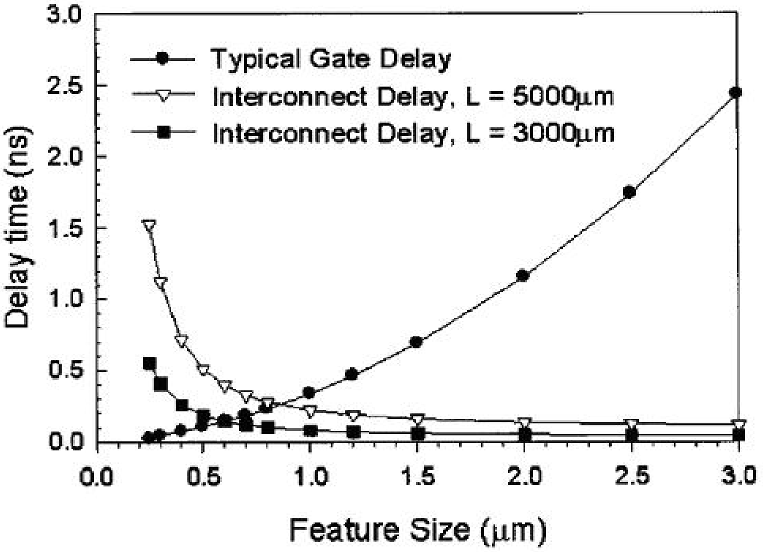

**Figure 1.1** Gate and interconnect delay versus feature size. Interconnect delay is shown for repeater spacings (L) of 3000 and 5000 μm [8].

by either lowering the interconnect wire resistance, or by reducing the capacitance of the interlayer dielectrics (ILD). The first change adopted by the industry was to lower the dielectric constant of $SiO_2$ from k = 3.9 to k =~ 3.5 by doping $SiO_2$ with fluorine. This fluorinated silica glass (FSG) resulted in modest gains [5]. A significant improvement was achieved by replacing the Al interconnect with Cu because of its low bulk electrical resistivity (Cu: 1.72 μΩ•cm, Al: 2.83 μΩ•cm) and superior resistance to electromigration [11]. The introduction of copper metallization enabled the aggressive interconnect scaling. Thinner metal wires could be used for copper versus aluminum wiring.

With copper reducing line and contact resistance, the next challenge is the reduction of parasitic capacitance. Because conductor spacing cannot be increased, the only way to reduce capacitance is to change ILD to new low permittivity (low-k) dielectrics. Carbon-doped silicon oxide and organic polymer materials with a k value of 2.6-2.8 have been developed for commercial applications [5,12-15]. New ultra low-k dielectrics such as porous materials are now in the stage of research and development [14-17]. The simulation shown in Figure 1.2 highlights the significant advantages of low-k dielectrics and Cu metallization versus Al and $SiO_2$ system for a typical microprocessor implementation [8]. Therefore, Cu/low-k technology has and continues to be a mainstream technology for sub-100 nm node ULSI circuit interconnect process.

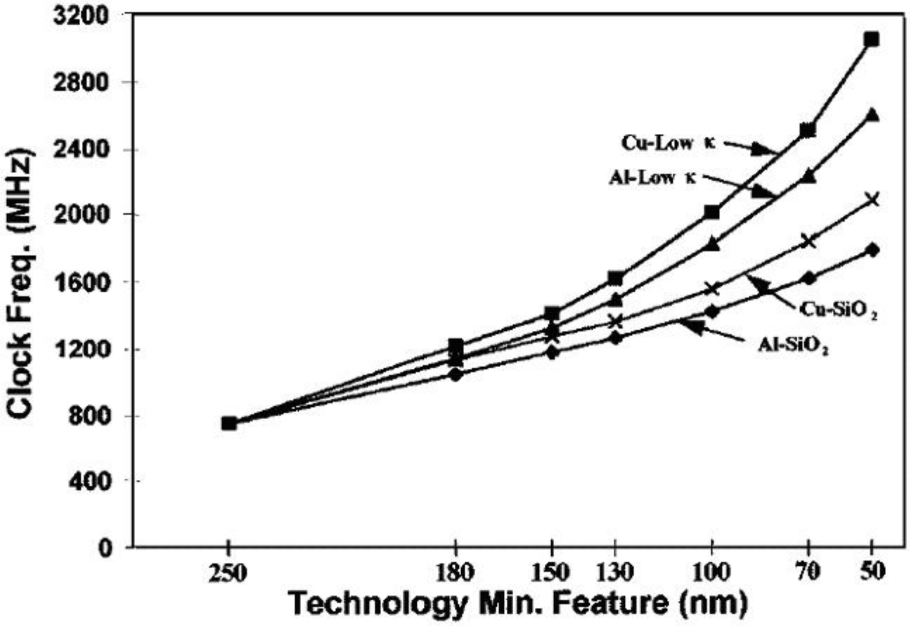

**Figure 1.2** Microprocessor performance as a function of feature size and interconnect technology (logic depth=12 gates) [8].

### 1.2.2 Copper interconnect fabrication – Dual damascene

The introduction of Cu into the interconnect, or back-end-of-line (BEOL), also caused a revolution on interconnect fabrication. Because Cu is very difficult to delineate by the traditional subtractive etching method due to the limited number of volatile copper compounds, a new process named dual damascene has been developed for the fabrication of Cu interconnect. Several different dual damascene integration schemes have been reported, but all approaches can generally be categorized as "via first" or "trench first". The "via first" approach is briefly described below as an example of the Cu dual damascene fabrication process [18].

First, a dielectric diffusion barrier, via level dielectric, an etch stop layer, the metal level dielectric, and a hard mask are sequentially deposited, as shown in Illustration 1.1 (a). Second, a via photoresist layer is coated on the wafer and then lithographically patterned. Third, an anisotropic etch dig a via hole through the hardmask, ILDs and the embedded etch stop layer, and stops at the bottom dielectric diffusion layer. (Illustration 1.1 (b)). Fourth, after stripping the via photoresist, a layer of trench photoresist is coated and lithographically patterned. Fifth, an anisotroptic etch cuts the surface hard mask, down through the metal level dielectrics, and stops on the embedded etch stop layer. A trench for the interconnect line is formed. (Illustration 1.1 (c)). Sixth, after stripping the trench

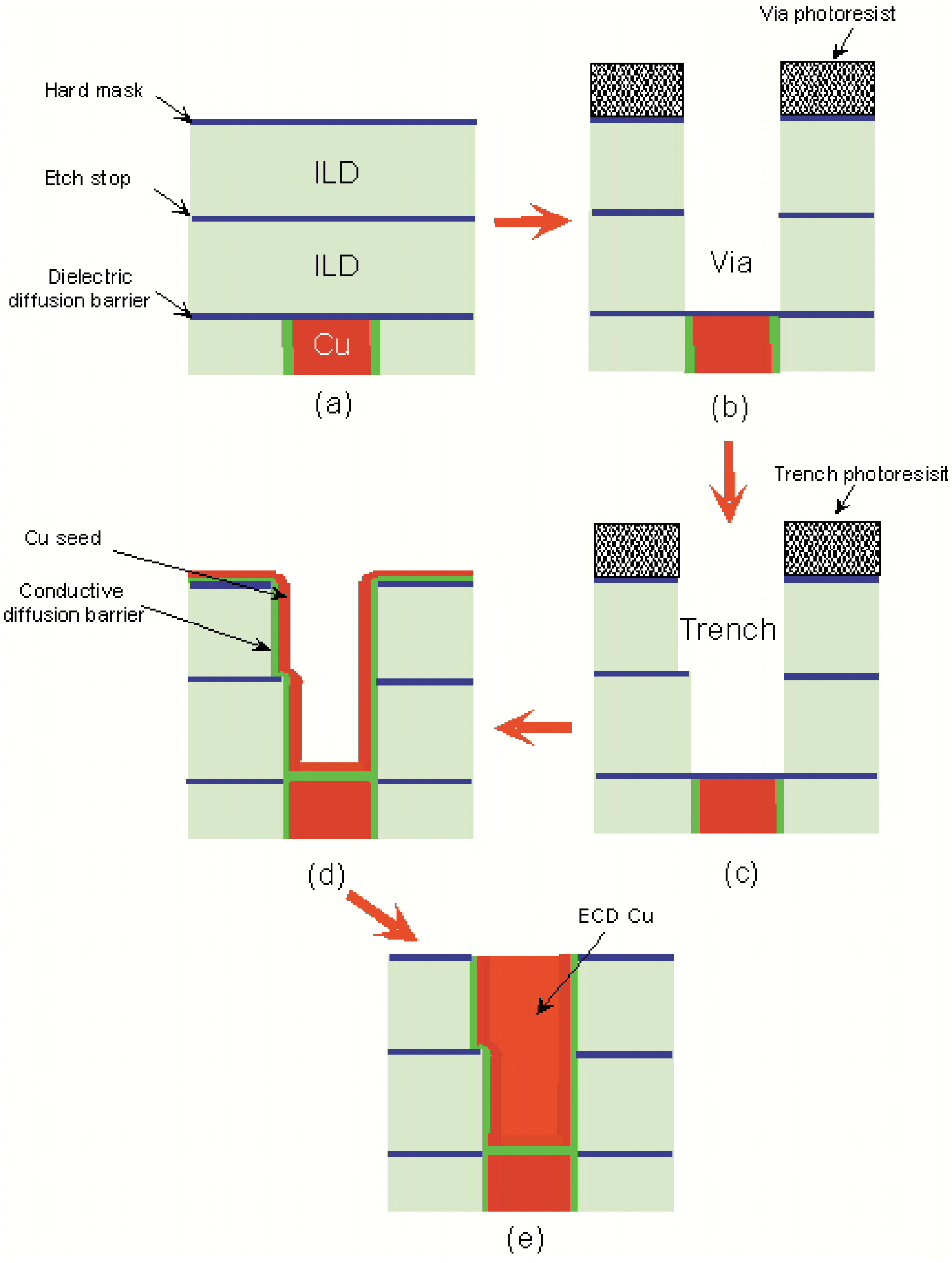

**Illustration 1.1** A process flow of Cu damascene fabrication ("via first")

resist and opening the dielectric barrier at the bottom of the via, a Cu diffusion barrier and a Cu seed layer are sequentially deposited along the sidewall and bottom of the trench and via. (Illustration 1.1 (d)) Finally, the bulk Cu is electroplated on the Cu seed layer, and it is polished back to the surface of the trenches, using chemical mechanical polishing (CMP). (Illustration 1.1 (e))

### 1.2.3 Deposition and characterization of copper diffusion barriers

When Cu was introduced to replace Al as the new interconnect material, it brought along several new problems. One of the toughest problems with implementing copper is its iteration with silicon and the dielectrics. It is well known that copper has fast diffusion in Si and it can react to form silicide [19-23]. Cu can also diffuse into $SiO_2$ and other dielectrics, which would cause the IC device failure. Moreover, Cu has poor adhesion properties with ILDs [24]. Therefore a conductive copper diffusion barrier film must be inserted between Cu and ILDs.

A good diffusion barrier should have these following attributes: first of all, it effectively prevents Cu diffusing into ILDs and other adjacent materials. Second, it should have a good conductivity to keep a low overall metal line resistance. Third, it can provide good adhesion to both Cu and ILDs, which is critical to resist delaminating during the subsequent processing and thermal stressing. Good adhesion can also help to improve copper eletromigration resistance. Fourth, a barrier film needs to uniformly and completely cover all of the sidewall and bottom of trenches and vias. Therefore, it is critical to develop a film deposition technology to grow a conformal barrier film on the non-planar interconnect architectures. Moreover, the barrier film should be smooth and free of defects, which significantly affects the quality of the subsequent Cu seed layer [1,12].

In recent years, many prospective barrier materials were widely studied, such as transition metals or alloy barriers, transition metal nitrides, carbide or oxide barriers, and transition metal silicide barriers [25-28]. Currently, tantalum (Ta) and tantalum nitride are used as the copper diffusion barrier for 90 nm node technology. Ionized physical vapor deposition (I-PVD) technology is typically used in the semiconductor industry to deposit the Ta/TaN barrier and Cu seed layer.

In order to prevent unexpected yield losses and avoid long-term reliability problems, the barrier films should be carefully tested for their barrier properties in preventing Cu diffusion [19,29]. Depth profiling techniques are traditionally used to characterize the effectiveness of Cu diffusion barriers. The most common depth-profiling techniques include secondary ion mass spectrometry (SIMS), Rutherford backscattering spectroscopy (RBS), X-ray photoelectron spectroscopy (XPS) and Auger electron spectroscopy (AES). Typically, a barrier and a Cu film are sequentially deposited on a $SiO_2$ or Si substrate. The sample is then annealed at elevated temperatures either in vacuum or in a forming gas ambient. The top Cu layer is etched away after annealing, and a Cu depth profile in the sample is analyzed by the above physical analysis technologies to see whether Cu has penetrated through the barrier and diffused into the substrate [30-39].

However, it has been found that a tiny amount of Cu, even for concentrations lower than the detection limit of physical analysis techniques, is sufficient to alter electrical characteristics of devices [19]. Therefore, several electrical test methods have been developed in past years, because these tests are more sensitive to detect barrier failure than the depth profiling methods. The basic principle of electrical test methods is to measure the change of electrical properties of a p-n junction, Schottky diode, or metal-oxide-semiconductor (MOS) capacitor when they are contaminated with Cu atoms [40-42]. For example, using a shadow mask, Cu/barrier metal dots are deposited on a thin $SiO_2$ film thermally grown on Si substrate. After thermal annealing, a shift of the original capacitance-voltage (C-V) curve of this MOS capacitor will indicate penetration of Cu through the barrier layer into the silicon dioxide [42-45].

### 1.2.4 Challenges on copper diffusion barrier for 45 nm node technology

When the IC feature size shrinks, the diffusion barrier needs to become thinner in order to decrease its impact on via contact resistance and the effective metal line resistance. According to ITRS prediction, the barrier thickness will scale to 5 nm or below in future 45 nm node technology [1]. It is challenging to completely prevent Cu from diffusing at a barrier thickness of 5 nm or less. Moreover, PVD technology is the current dominant technology for barrier and Cu seed layer deposition, but it may not be extendable to 45 nm node because of its poor step coverage on the high aspect ratio of trenches and via holes. Neither barrier material nor deposition technology is known for 45 nm node interconnect [1].

In this dissertation, Ruthenium (Ru) was studied as a promising barrier candidate for Cu ULSI interconnect. Ru is a transition metal with low electrical resistivity and high thermal stability. It doesn't oxidize readily, and ruthenium oxide is still a conductor [46]. The insolubility of Ru with Cu is a favorable attribute for a barrier material [47]. More importantly, it has been reported that Cu can electrolytically plate onto Ru [48]. Therefore, not only could Ru potentially become a diffusion barrier, but it could replace the Cu seed layer. All of the above benefits make Ru a very attractive barrier material. My work on chemical vapor deposition (CVD) and characterization of thin Ru films on Ta and $SiO_2$ are reported in chapter 4 and 5.

## 1.3 Objective and chapter overview

The goal of the research presented here is to study deposition and properties of thin metal and metal oxide films for the application in the next generations of integrated circuit fabrication. It includes deposition of the $Al/Al_2O_3$ film as a potential thermal resist for e-beam projection lithography; development of a real time surface analysis system for *in-situ* surface chemistry studies, thin film reaction and diffusion kinetics at elevated temperatures; and deposition and characterization of CVD Ru films, the latter used as a potential Cu diffusion barrier for 45 nm node Cu interconnect. Chapters 2 through 5 cover the details of these above works, and Chapter 6 summarizes the accomplishments in this dissertation and recommendations for future work.

Chapter 1 describes deposition of $Al/Al_2O_3$ cermet films and investigation of the mechanism of their transformations induced by laser irradiation. 100 nm thick $Al/Al_2O_3$ cermet films, which consist of 15.5% Al and 84.5% $Al_2O_3$, were deposited by reactive sputter deposition. These cermet films were then irradiated in vacuum and air by a single 7 ns pulse from a 1064 nm laser. Characterization included X-ray photoelectron spectroscopy, scanning electron microscopy and atomic force microscopy. Irradiation in vacuum led to re-distribution of components within the first ~35 nm beneath the surface. Irradiation in air increased the concentration of $Al_2O_3$ in the same region. Irradiation increased the

RMS surface roughness by a factor of 10 in both environments (from 3.5 to 36 nm). On the other hand, Al films irradiated in air do not oxidize measurably with a single laser pulse. Model calculations indicate that a single laser pulse (~16 MW cm$^{-2}$) can increase the local temperature of cermet from 300 to 1200 K. We interpret the observed transformations as a result of local heating and, in air, as accompanying thermal oxidation.

Chapter 3 describes a novel *in-situ* laser annealing system for real time surface kinetic analysis. A continuous wave $CO_2$ infrared laser was coupled to a surface analysis system equipped for x-ray photoelectron spectroscopy and ion scattering spectroscopy. The laser beam was directed into the vacuum chamber through a ZnSe window to the back side of the sample. With 10 W laser output, the sample temperature reached 563 K. The chamber remained below $10^{-8}$ Torr during annealing and allowed XPS and ISS data to be gathered as a function of time at selected temperatures. This system works well for any sample, conducting, semi-conducting or insulating, that absorbs the 10 μm laser radiation. Using this system, real time $Cu_2O$ reduction at 563 K was investigated.

Chapter 4 explores a low temperature thermal CVD route to grow Ru thin films using $Ru_3(CO)_{12}$ precursor. Pure, smooth and uniform Ru films on Ta and low resistivity films on $SiO_2$ were grown by thermal CVD at temperatures as low as 423 K (150 °C). Measured using XPS and ISS, a 2.5 nm Ru film fully covers underlying Ta, and the Ru/Ta interface is thermally stable up to at least 573 K. A

6 nm Ru film can be an effective oxygen barrier to prevent underlying Ta from oxidation when subjected to conditions of either high vacuum annealing or exposure to ambient air. In contrast to Ta, the Ru film exhibits excellent wettability by Cu even when the Ru surface is contaminated with small amounts of oxygen.

Chapter 5 reports pure and polycrystalline Ru film deposition $SiO_2$ by the same thermal CVD process using $Ru_3(CO)_{12}$. The CVD Ru film is thermally stable up to 673 K and has good adhesion properties with Cu and $SiO_2$, but the Ru film exhibits poor step coverage on patterned $SiO_2$. A 4 nm Ru film and a 2.9 nm Ru/0.6 nm Ta composite film are effective copper diffusion barriers under 60 min annealing at 623 K in $H_2$(10%)/$N_2$ ambient. In chapter 4 and 5, except when indicating those measured by SEM, all other Ru film thicknesses were measured using XPS substrate peak attenuation.

## 1.4 References

[1] International Technology Roadmap for Semiconductors, 2001 Edition, http://public.itrs.net/, (2001)

[2] S. Nonogaki, T. Ueno, and T. Ito, Microlithography: Fundamentals in Semiconductor Devices and Fabrication Technology (New York Marcel Dekker, Inc., New York, NJ, 1998)

[3] T Brunner, IEDM, IEEE, 9 (1997)

[4] J. Canning, Int. conference on microelectronic test structures, IEEE **11**, 25 (1998)

[5] M. P. Petkov, Low-k interlevel dielectrics technology, http://nepp.nasa.gov/index_nasa.cfm/810/

[6] J. D. Plummer, M. D. Deal, and P. B. Griffin, Silicon VLSI Technology Fundamentals, Practice and Modeling (Prentice Hall, Upper Saddle River, NJ, 2000).

[7] A. M. Lemonds, Ph. D Dissertation, The University of Texas at Austin, (2003)

[8] R. H. Havemann and J. A. Hutchby, Proc. of IEEE **89**, 586 (2001)

[9] J. P. Chang, C. B. Case, H. W. Krautter, J. Sapjeta, R. L. Opila, and M. A. Decker, Proc. Electrochem. Soc. **99**, 261 (1999)

[10] C. Whitman, M. M. Moslehi, A. Paranjpe, L. Velo, and T. Omstead, J. Vac. Sci. Technol. A **17** 1893 (1999).

[11] M. Kwak, D. Shin, T. Kang and K. Kim, Thin Solid Films **339,** 290 (1999)

[12] P. Singer, Semiconductor International, **25**, 46 (2002)

[13] L. Peters, Semiconductor International, **24**, 66 (2001)

[14] L. Peters, Semiconductor International, **25**, 55 (2002)

[15] K. Maex, M. R. Baklanov, D. Shamiryan, F. Lacopi, S. H. Brongersma, and Z. S. Yanovitskaya, J. Appl. Phys., **93**, 8793, (2003)

[16] J. Golden, C. Hawker, and P. Ho, Semiconductor International, **24**, 79 (2001)

[17] C. Jezewski, W. A. Lanford, C. J. Wiegand, J. J. Senkevich, T. Lu, Semiconductor International, **27**, 56 (2004)

[18] S. Wolf, Silicon Processing for the VLSI Era, Vol. 4 Deep-Submicron Process Technology (Lattice Press, Sunset Beach, CA, 2002)

[19] Istratov, C. Flink and E. Weber, Phys. Stat. Sol. B, **222**, 261 (2000)

[20] K.-H. Min, K.-C. Chun, and K.-B. Kim, J. Vac. Sci. Technol. B **14**, 3263 (1996)

[21] T. Laurila, K. Zeng, J. K. Kivilahti, J. Molarius, and I. Suni, J. Appl. Phys. **88**, 3377 (2000)

[22] C. S. Lee, H. Gong, R. Liu, A. T. S. Wee, C. L. Cha, A. See, and L. Chan, J. of Appl. Phys. **90**, 3822 (2001)

[23] T. Oku, E. Kawakami, M. Uekubo, K. Takahiro, S. Yamaguchi, and M. Murkami, Appl. Surf. Sci. **99**,265 (1996)

[24] H. Kizil, G. Kim, C. Steinbruchel and B. Zhao, J. Electron. Mat. **30**, 345 (2001)

[25] S. Wang, MRS bull. **19**, 30 (1994)

[26] Y. Shacham-Diamand, J. Electro. Mat. **30**, 336 (2001)

[27] F. Braud, J. Torres, J. Palleau, J. Mermet and M. Mouche, Appl. Surf. Sci. **91**, 251 (1995)

[28] M. Wang, L. Chen and M. Chen, J. Electrochem. Soc. **146**, 728 (1999)

[29] A. Istratov and E. Weber, J. Electrochem. Soc. **149**, G21 (2002)

[30] A. Kaloyeros, C.Xiaomeng, T. Stark, K. Kumar, S. Soon-Cheon, G. Peterson, H. Frisch, B. Arkles and J. Sullivan, J. Electrochem. Soc. **146**, 170 (1999)

[31] M. Kwak, D. Shin, T. Kang and K. Kim, J. Appl. Phys. **38**, 5792 (1999)

[32] S. Wang, H. Tsai, S. Sun, J. Appl. Phys. **40**, 2642 (2001)

[33] R. Koger, M. Eizenberg, D. Cong, N. Yoshida, L. Chen, S. Ramaswami, D. Carl, Microeletron. Eng. **50**, 375 (2000)

[34] L. Liu, H. Gong, Y. Wang, A. Wee, R. Liu, Int. J. Modern Phys. B **16**, 322 (2002)

[35] Y.-M. Sun, S. Y. Lee, A. Lemonds, J. Lozano, J.-P. Zhou, J. G. Ekerdt, J. M. White, I. Imesh, Surf. Interface Anal. **32**, 79 (2001)

[36] Y. K. Lee, M L. Khin, J. Kim, K. Lee, Mat. Sci. Semicond. Processing, **3**, 179 (2000)

[37] W. H. Teh, L. T. Koh, S. M. Chen, J. Xie, C. Y. Li, P. D. Foo, Electron. Lett. **37**, 660 (2001)

[38] A. Kohn, M. Eizenberg, Y. Shacham-Diamand, B. Israel, Y. Sverdlov, Microelectron. Eng. **55**, 297 (2001)

[39] W. Qin, Z. Q. Mo, L. J. Tang, B. Yu, S. R. Wang, J. Xie, J. Vac. Sci. TEchnol. B **19**, 1942 (2001)

[40] J.-C. Chuang, S.-L. Tu and M.-C. Chen, J. Electrochem. Soc. **146**, 2643 (1999)

[41] C. Ahrens, R. Ferretti, G. Friese and J. O. Weidner, Microelectron. Eng. **37/38**, 211 (1997)

[42] S. K. Rha, W. J. Lee, S. Y. Lee, Y. S. Hwang, Y. J. Lee, D. I. Kim, D. W. Kim, S. S. Chun and C. O. Park, Thin Solid Films **320**, 134 (1998)

[43] F. Braud, J. Torres, J. Palleau, J. L. Mermet and M. J. Mouche, Appl. Surf. Sci. **91**, 251 (1995)

[44] F. Braud, J. Torres, J. Palleau, J. L. Mermet, C. Marcadal and E. Richard, Microelectron. Eng. **33**, 293 (1997)

[45] M. Y. Kwak, D. H. Shin, T. W. Kwang and K. N. Kim Phys. Stat. Sol. (a) **174**, R5 (1999)

[46] J. Emsley, The Elements, 3rd ed. (Oxford, 1998)

[47] T. B. Massalski, Editor, Binary Alloy Phase Diagram, 2nd ed., (Materials Information Society, Material Park, OH, 1990)

[48] O. Chyan, T. N. Arunagiri, and T. Ponnuswamy, J. Electrochem. Soc. **150**, C347 (2003)

# Chapter 2

# Al/$Al_2O_3$ film growth and laser induced transformation

## 2.1 Introduction

Modern microelectronics manufacturing involves ever-shrinking device dimensions that place increasing demands on existing lithography processes. As integrated circuit technology approaches the 100 nm generation (100 nm lines/spaces for DRAMS, 70 nm isolated gates for logic), optical lithography becomes more difficult and may reach a limit. Thus, other technologies are competing to demonstrate patterning capability at these and smaller dimensions; examples include using lasers, X-rays, e-beams and ions in a variety of imaginative ways for lithography [1-5]. Implementation of these will likely require significant changes in materials and processes. In the materials arena, pursuit of new resist materials is worthwhile since traditional resists for photochemically based photolithography may not be applicable. For example, e-beam or ion projection lithography requires a thermally active resistance, and to be applicable, it must be highly sensitive and capable of improving spatial resolution [5].

Cermets, mixtures of metal particles in a metal oxide matrix, or the reverse, are candidate materials that have not been thoroughly considered, and in this paper, we report on one member of this class—Al mixed with $Al_2O_3$. Such metal–dielectric composites are of interest as resists for patterning because their chemical (e.g. etch resistance) properties can be altered by exposure to laser or ion irradiation. It is known, for example, that the nitric acid etching rate of an $Al/Al_2O_3$ cermet is much slower, by as much as a factor of 2, after the cermet has been exposed to 193 nm laser radiation [6-8]. Of course, other properties such as roughness and particle size must be evaluated to establish viability as a resist.

Previous work has not focused on the mechanism of the transformation induced by the irradiation. For laser-induced changes, possibilities include phase transformation, photon-induced reaction and thermal reaction. In this paper, we present and discuss unambiguous evidence for thermal transformations of the $Al/Al_2O_3$ cermet by using a 1064 nm infrared laser that does not induce electronic excitations. X-ray photoelectron spectroscopy (XPS) was used to analyze film composition, atomic force microscopy (AFM) to assess surface roughness, and scanning electron microscopy (SEM) to determine film thickness and film particle sizes. Model calculations demonstrate that the local temperature rise due to thermal heating is sufficient to melt Al, and a model is proposed for thermally induced changes that involve movement of the $Al_2O_3$ particles within liquefied Al and when $O_2$(gas) is present, oxidation of Al.

## 2.2 Experimental

### 2.2.1 Film deposition tools and conditions

$Al/Al_2O_3$ cermets were deposited at 300 K on a clean Si(1 0 0) wafer in a plasma sputter deposition system (AJA 1500H) comprising a load lock chamber and a main chamber ($<5\times10^{-8}$ Torr) with three sputter guns, one DC and two RF power supplies. The substrate could be heated to 773 K using a quartz lamp.

Reactive sputtering from a metallic Al target used 40 sccm, ultra-high pure Ar gas (99.999%) directly injected into the sputter gun operating at 180 W DC power. The total chamber pressure during film growth was maintained at 8 mTorr. When oxide was grown, $O_2$ was injected simultaneously; 10% $O_2$ diluted in Ar was backfilled with a flow rate of 5 sccm. By controlling the oxygen-to-argon flow ratio, we could vary the aluminum-to-aluminum oxide ratio in the cermet films from 0.05 to 0.33. To test the effects of laser irradiation, we chose $[Al^0]/[Al^{3+}]=0.17$.

### 2.2.2 Materials

The aluminum target (99.7% pure) was purchased from PureTech. The certified standard Ar and $O_2$ gases were purchased from Praxair. Boron-doped Si(1 0 0) wafers, 100 mm in diameter and ~0.5 mm thick, were purchased from MEMC. Surface hydrocarbons were removed using acetone, isopropyl alcohol and deionized water in sequential washings. The native oxide was removed with HF.

### 2.2.3 1064 nm infrared laser

For the set of experiments reported here, a pulsed IR YAG laser (Continuum Powerlite 7010) delivered one pulse of 1064 nm irradiation, normal to the sample surface, cermet or pure Al in either air or vacuum. For the latter, a mechanically pumped chamber ($5\times10^{-2}$ Torr) was used. Single pulses of 2, 3.5 and 5.0 mJ were delivered in 7 ns to a 0.031 $\mathrm{cm}^2$ spot, i.e. laser power density between 9.2 and 23.0 MW $\mathrm{cm}^{-2}$.

### 2.2.4 Analysis

The film composition was analyzed using a PHI 5600 X-ray photoelectron spectrometer employing monochromatic Al K$\alpha$ X-rays and operated at pass energies 93.9 eV for surveys and 11.75 eV for high-resolution scans. For depth profiles, the films were sputtered with 2 kV Ar ions at a sample current of 1 $\mu$A.

The film surface roughness and morphology were investigated with Thermomicroscopes Autoprobe atomic force microscope operated in laboratory at ambient atmosphere and in the intermittent contact (IC) mode. Si probe tips with force constants between 2.0 and 3.5 N $\mathrm{m}^{-1}$ were used. The RMS roughness values of multiple images were averaged. The film particle size and thickness were determined using a LEO 1530 SEM operated at 100k× magnification.

## 2.3 Results

### 2.3.1 $Al/Al_2O_3$ cermet deposition on Si(1 0 0)

To prepare films that were not fully oxidized, i.e. to prepare useful $Al/Al_2O_3$ cermets, it was necessary to use less than 0.5 sccm $O_2$ flow with 44.5 sccm of Ar. At this low $O_2$ flow rate, plasma uniformity and stability problems arise when oxygen first begins flowing into the chamber; the resulting films exhibit uneven lateral composition on the $mm^2$ area scale probed by XPS. This problem was alleviated by preconditioning the metal target; the Al target was sputtered for 10 min in Ar and 10 min in $Ar+O_2$ before depositing the film. The resulting films were uniform to within 5%—100±5 nm thick as measured by SEM.

XPS (Figure 2.1) of a cermet film—as-deposited (a) and after removing 10 nm of material (b)—exhibits peaks originating from ejection of Al 2p, Al 2s, O 1s, Ar 2s, Ar 2p and C 1s core electrons. In addition, the O(KLL) Auger signals are easily identified. While (a) has a relatively intense C 1s contribution, (b) does not, indicating that the bulk cermet film is composed only of Al and $Al_2O_3$, and carbon is limited to the surface and accumulated during post-deposition sample handling.

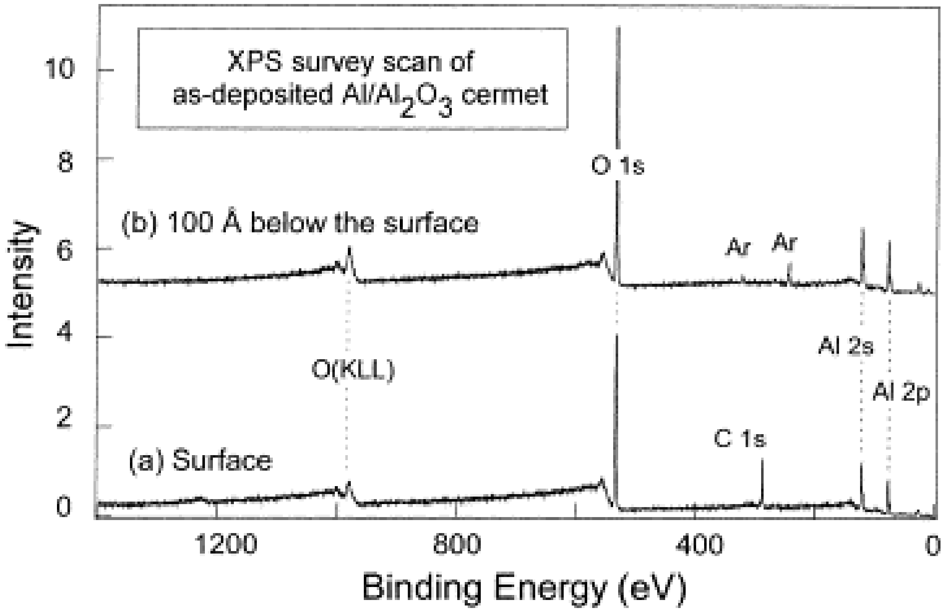

**Figure 2.1** Survey XPS of an Al/$Al_2O_3$ cermet grown by plasma sputter deposition on Si(1 0 0). Growth conditions were 300 K, 8 mTorr total pressure, 180 W DC power, 40 sccm Ar flow and 0.5 sccm $O_2$ flow. Spectrum: (a) as-deposited film; (b) after removal of ~10 nm of surface material.

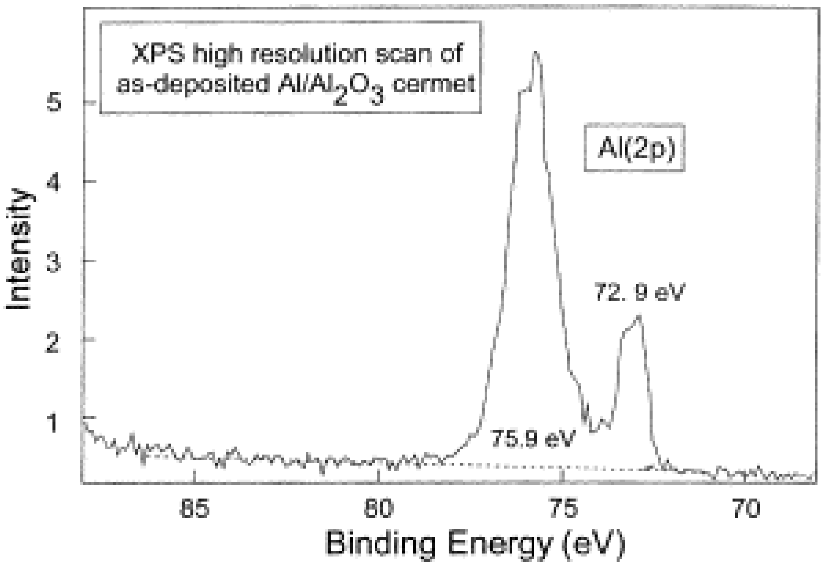

**Figure 2.2** Al 2p XPS of as-deposited Al/$Al_2O_3$ cermet (conditions same as in Figure 2.1).

A high-resolution scan of the Al 2p region (Figure 2.2) of the as-deposited film establishes the cermet character of the film, i.e. a metallic aluminum peak at 72.9 eV binding energy (BE) and an oxidized Al peak at 75.9 eV BE. To establish the bulk composition, the $[Al^0]/[Al^{3+}]$ ratio was calculated by rationing the integrated intensities of these two peaks as a function of the $Ar^+$ sputtering time in the XPS machine. The resulting depth profile, shown as diamonds in Figure 2.3, indicates a stable $[Al^0]/[Al^{3+}]$ ratio of 0.2 except for the topmost 5 nm. The outermost region is richer in $Al^0$, a result attributable to the way we terminated film growth; the 180 W DC power bias on the sputtering gun was turned off gradually over 3–4 min since quickly terminating the DC power induces a sharp temperature drop in the aluminum target tending to damage it. During this procedure, more unoxidized Al is deposited. Preferential sputtering reaching steady-state was ruled out on the basis of the data taken without any sputtering and the laser irradiation results described below.

The RMS roughness (3.52 nm) of this $Al/Al_2O_3$ cermet was calculated from multiple 30 μm×30 μm AFM images, one of which is shown in Figure 2.4(a) along with a line scan. The films were black indicating strong scattering of light. An SEM image, Figure 2.5(a), shows that the average particle diameter in this cermet film is less than 30 nm.

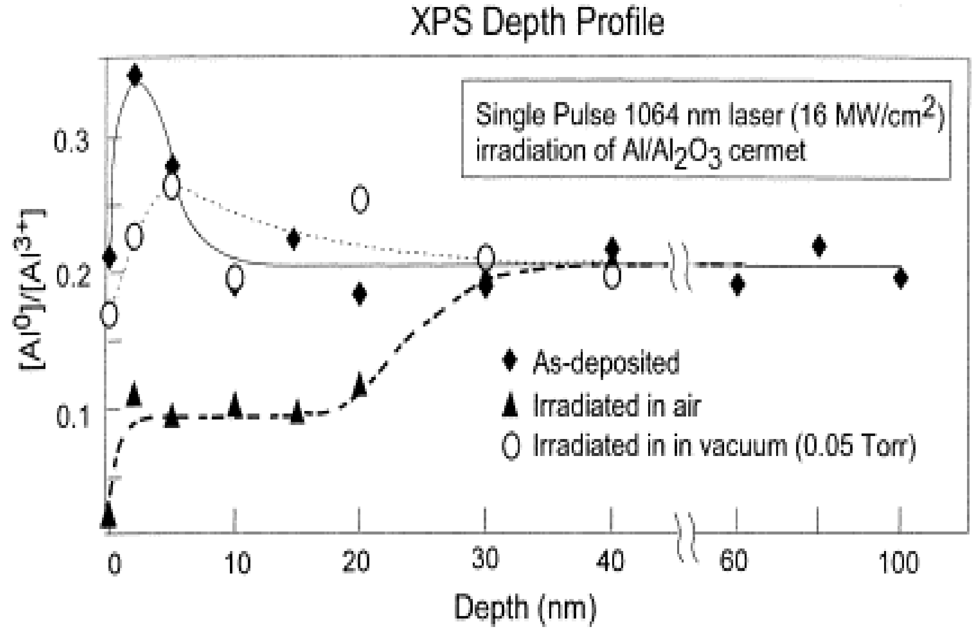

**Figure 2.3** XPS depth profiles of an Al/$Al_2O_3$ cermet prepared as in Figure 2.1: (♦) as-deposited, and irradiated with a single pulse from a 1064 nm laser in (▲) ambient air and (○) vacuum of $5\times10^{-2}$ Torr. The laser power density was 16.1 MW $cm^{-2}$ based on 3.5 mJ delivered in 7 ns to 0.031 $cm^2$.

### 2.3.2 The effects of laser irradiation on Al/$Al_2O_3$

A single 1064 nm laser pulse with a power density of ~16 MW $cm^{-2}$ in air caused a color change from black to light blue localized at the point of irradiation. The XPS depth profile (triangles in Figure 2.3) differs strongly from the as-deposited film (diamonds). The surface (~1 nm) was fully oxidized; $Al^0$ was below XPS detection limits (<1%). Furthermore, the region between 2 and 20 nm was of nearly constant composition ($[Al^0]/[Al^{3+}]$=0.10), i.e. half that of the as-deposited film. Finally, between 20 and 30 nm, the $[Al^0]/[Al^{3+}]$ ratio rises to 0.20, the value for the as-deposited film.

Figure 2.4(b) shows an AFM image and a line scan of the irradiated area; this surface is 10 times rougher than the as-deposited film (RMS roughness=36 vs. 3.5 nm). In addition and consistent with the color change, numerous closely spaced large diameter particles, ~150 nm, were evident. The SEM image, shown in Figure 2.5(b), reveals many particles with diameters up to 150 nm. This is significantly different from the as-deposited film where particle diameters are much smaller, ~25 nm or less.

Unlike the ~16 MW $cm^{-2}$ pulse, a power density of ~9 MW $cm^{-2}$ caused a color change from black to light brown. The XPS depth profile (circles in Figure 2.6) indicates that the $[Al^0]/[Al^{3+}]$ ratio in the top 10 nm layer lies between that of the as-deposited film and the film irradiated with ~16 MW $cm^{-2}$ pulse. On the

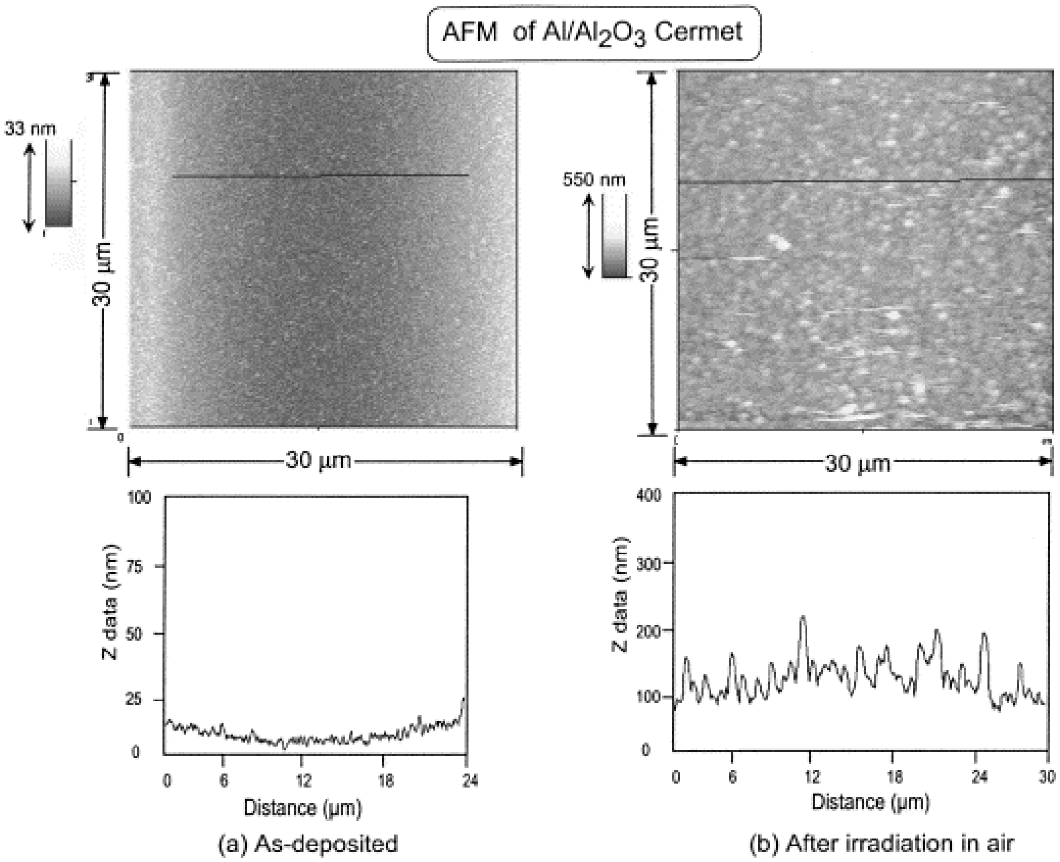

**Figure 2.4** AFM images of an $Al/Al_2O_3$ cermet: (a) as-deposited; (b) irradiated with a 16.1 MW cm$^{-2}$, 1064 nm laser pulse in air.

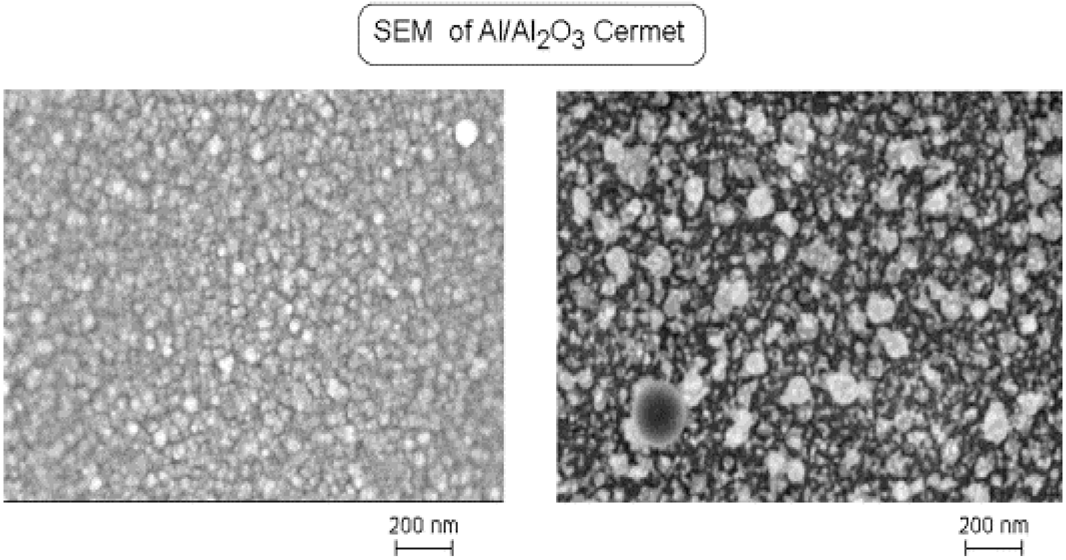

(a) As- deposited

(b) After irradiation in air

**Figure 2.5** SEM images of an Al/Al$_2$O$_3$ cermet: (a) as-deposited; (b) irradiated with a single 16.1 MW cm$^{-2}$, 1064 nm laser pulse in air.

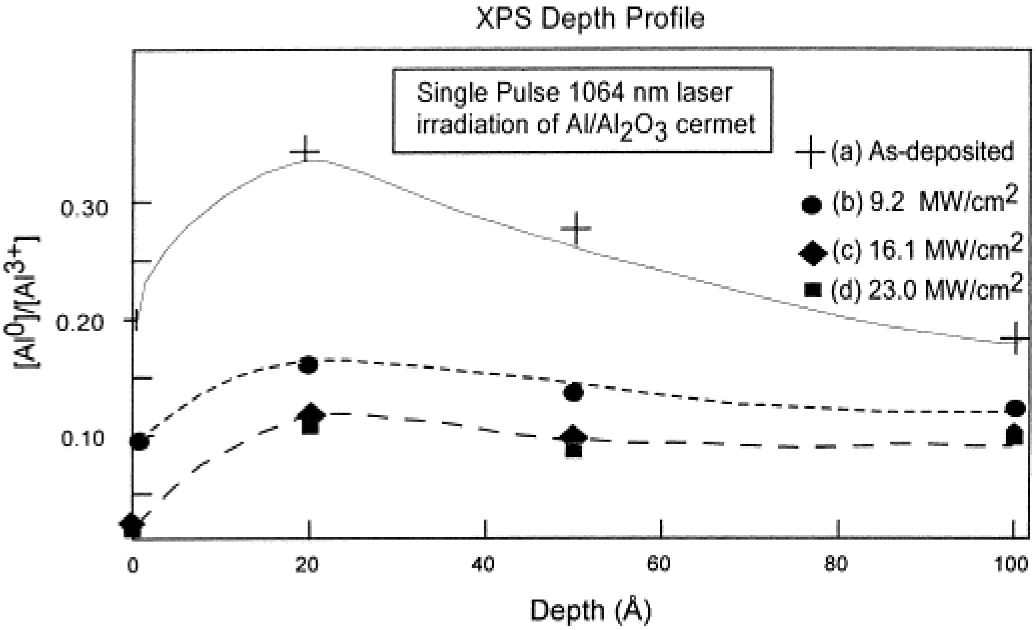

**Figure 2.6** XPS depth profiles of an Al/Al$_2$O$_3$ cermet prepared as in Figure 2.1: (a) as-deposited or irradiated with a single 1064 nm laser pulse in ambient air at power densities of (b) 9.2, (c) 16.1 and (d) 23.0 MW cm$^{-2}$.

other hand, irradiation with a power density of ~23 MW $cm^{-2}$ produced the same black to blue color transformation, and XPS shows the same $[Al^0]/[Al^{3+}]$ ratio as with ~16 MW $cm^{-2}$ laser power.

Irradiation in vacuum (single pulse) produced the same black to blue color transformation as irradiation in air indicating a similar change in particle size. However, significant differences are discernible in XPS (circles in Figure 2.3). Most importantly, there is no broad region where the $[Al^0]/[Al^{3+}]$ ratio lies below that of the as-deposited film. Although the outermost 5 nm $[Al^0]/[Al^{3+}]$ ratios are lower, the depth profile for 5 nm and beyond is indistinguishable from that of the as-deposited film; the ratio becomes 0.2 for all depths beyond 10 nm. The RMS roughness of this sample was, like that for the sample irradiated in air, tenfold larger than that for the as-deposited system (not shown).

### 2.3.3 Irradiation of aluminum

For comparison, we prepared and irradiated a 100 nm thick film of aluminum in air. A single laser pulse does not visibly alter the film, and the XPS depth profiles of the film before and after laser irradiation are superimposable (Figure 2.7). Despite significant $Al^{3+}$ at the surface, pure Al is reached at 2 nm in both cases. Unlike cermets, the metal Al films in air do not oxidize measurably with a single laser pulse.

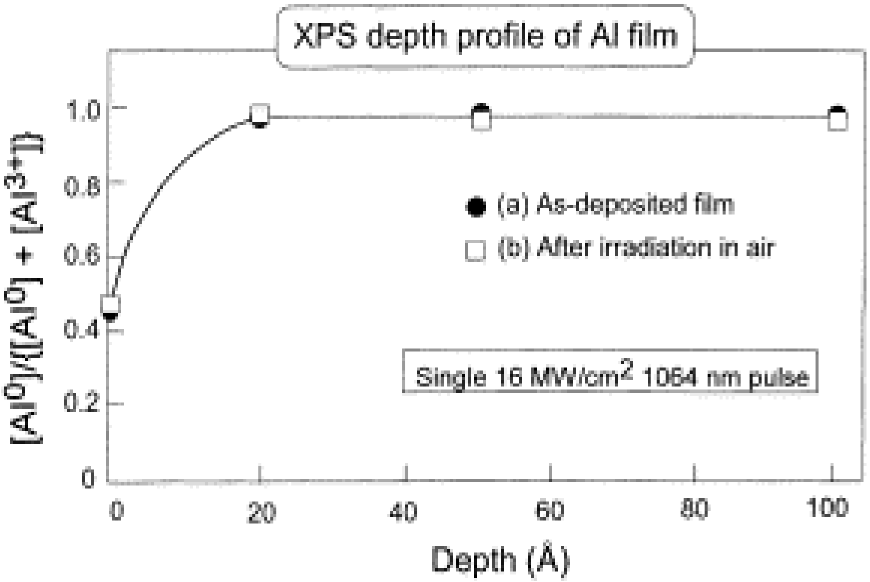

**Figure 2.7** XPS depth profiles of an Al film deposited on Si(1 0 0): (a) as-deposited; (b) single laser pulse in air with power density=16.1 MWcm$^{-2}$. Growth conditions were: 300 K, 8 mTorr total pressure, 180 W DC power and 40 sccm Ar flow.

## 2.4 Discussion

### 2.4.1 Surface temperature rise during laser irradiation

Since electronic excitations do not occur in the Al/$Al_2O_3$ cermet when using the photon energy of 1064 nm radiation used here, the changes are limited to thermal effects. It is instructive to estimate the laser-induced temperature rise and fall that accompanies a single laser pulse. The time-dependent temperature variation can be calculated using a classical heat conduction equation, the thermal properties of the solid (Table 2.1) and the boundary value conditions for laser heating [9]. Treating the laser pulse as a surface heat source and treating heat flow in one dimension into the solid, the time dependence of the surface temperature is

$$\Delta T(t) = \left(\frac{F_0}{K}\right)\left(\frac{\kappa}{\pi}\right)^{1/2} \int_0^t A(t-\tau)\tau^{-1/2}d\tau \tag{1}$$

where $A(t)$ is the normalized laser pulse shape, $F_0$ the maximum absorbed laser power density, $K$ the thermal conductivity and $\kappa$ the thermal diffusivity of the solid. $K$ and $\kappa$ are assumed to be temperature independent. The maximum surface temperature rise ($\Delta T$) due to heating by a temporally square laser pulse of length $t_0$ is

$$\Delta T_m = 2\left(\frac{F_0}{K}\right)\left(\frac{\kappa t_0}{\pi}\right)^{1/2} \tag{2}$$

According to Fresnel's equations for reflection, if the incident beam is perpendicular to the surface, the normal incidence reflection $R$ in air is given by

$$R = \frac{(n-1)^2 + k^2}{(n+1)^2 + k^2} \tag{3}$$

where $n$ and $k$ are the refractive index and extinction coefficient, respectively, of the medium adjacent to the reflecting surface [10]. Assuming, for estimation purposes, $n$ and $k$ of bulk Al and $Al_2O_3$ at 1064 nm (Table 2.1), we calculate normal incidence reflections of $R_{Al}$=0.9569 and $R_{Al2O3}$=0.0750 indicating, as expected, that $Al_2O_3$ absorbs most of the incident energy, while metallic Al absorbs very little. The estimated maximum absorbed laser power density $F_0$ is

$$F_0 = F \times [C_{Al_2O_3} \times (1 - R_{Al_2O_3}) + C_{Al} \times (1 - R_{Al})] = 12.69\ \mathrm{MW/cm^2}$$

where $F$=16.1 MWcm$^{-2}$, and $C_{Al2O3}$ and $C_{Al}$ are the concentrations of $Al_2O_3$ and Al, respectively, in the as-deposited cermet. Using these parameters, the maximum surface temperature is 1200 K. While use of bulk optical constants is clearly approximate, it is also the case that changes of ±20% introduce only a 50 K change in the estimate.

Furthermore, according to Beer's law, the energy absorbed as a function of depth into the material is given as

$$\frac{I}{I_0} = \exp(-\alpha z) \tag{4}$$

where $I_0$ and $I$ are, respectively, the absorbed energy at the surface and after traversing a distance $z$ in the film. The absorption coefficient of the film $\alpha$ is defined as

$$\alpha = 4\pi k / \lambda \qquad (5)$$

where $k$ is the extinction coefficient of the film and $\lambda$ is the incident laser wavelength. From Eq. (4), when $z$=20 nm, the absorbed radiant energy is only ~70% of that on the surface, and the calculated maximum temperature at a depth of 20 nm is 950 K.

**Table 2.1 Some Physical, Thermal and Optical Properties of Al and $Al_2O_3$ [11,12]**

| | Melting Point (K) | Boiling Point (K) | Heat Capacity (J/mol K) (25 ° C) | Thermal conductivity (W / m K) (25 ° C) | Thermal Diffusivity ($mm^2/s$) (25 ° C) | Index of Refraction n (1064nm) | Extinction of Coefficient k (1064nm) |
|---|---|---|---|---|---|---|---|
| Al | 933.47 | 2792.15 | 24.2 | 235 | 97.04 | 1.237 | 10.478 |
| $Al_2O_3$ | 2327.15 | ≅3273.15 | 79.0 | 34.25 | 11.13 | 1.754 | ~0 |

### 2.4.2 Mechanism of $Al/Al_2O_3$ cermet transformation during laser irradiation

Because the primary component of the cermet film is $Al_2O_3$, which absorbs strongly at 1064 nm, most of the IR absorption excites phonons in $Al_2O_3$ to temperatures above 1200 K. Subsequently, energy flows into modes associated with Al and the interfaces between the two materials.

First, we discuss the process under vacuum. A microscopic description involving the time-dependent mass and energy flow is very complex, so we resort to rough qualitative descriptions. As the laser pulse raises the average $T$ to around 1200 K, the heated $Al_2O_3$ particles expand and as energy transfers to the Al particles, they expand, melt (933 K) and flow. Melting occurs only in top ~20 nm layer of the film, since temperatures further into the sample are below the melting point of Al. This melt zone can expand mainly only perpendicular to the surface, since it is bounded by solid material in all other directions. Energy can be transferred in various ways in all directions.

Because the film deposition ended by depositing Al in the absence of $O_2$, the $[Al^0]/[Al^{3+}]$ ratio in the top 2 nm of the as-deposited film is about 1.7 times deeper within the cermet. In vacuum, this Al concentration gradient could be reduced by molten Al flow from this region deeper into the film, thereby enriching the outermost region in $Al_2O_3$. Other factors, e.g. density and surface tension, may provide competing or amplifying driving forces. When the laser pulse ends, the film temperature decreases sharply and all the particles are frozen in a new state, likely kinetically, not thermodynamically controlled. These transient thermal movements evidently increase the surface roughness by a factor of 10 and induce a re-distribution of components in the top 35 nm layer. Any $Al^0$ that moved to the exposed surface aluminum is quickly oxidized during sample transfer for *ex situ* XPS analysis.

Turning to irradiation in air, we note that because excess $O_2$ is present, a different result is obtained, Al is oxidized. So long as Al remains molten, oxidation can proceed through continual movement of Al atoms to the air–liquid interface. Accordingly, large amounts of aluminum in the top layer are oxidized by a 7 ns FWHM laser pulse that produces a temperature pulse about 15 ns long. Consistent with the above calculation, oxidation extends only 20–30 nm into the film, since the maximum temperature of layers below 20 nm is already lower than the Al melting point and oxygen diffusion in solid $Al_2O_3$ is negligible for these time–temperature conditions [13-14].

Considering the variation with laser pulse power density, it is noteworthy that the extent of oxidation increases significantly between 9 and 16 MW $cm^{-2}$ but not between 16 and 23 MW $cm^{-2}$. The increase is consistent with expectations that the rate will depend exponentially on the temperature provided the rate is controlled by the same step in the reaction path. That oxidation does not change between 16 and 23 MW $cm^{-2}$ indicates that control changes. We take this as indicating that, while the maximum temperature reached is higher for 23 MW $cm^{-2}$, the extent of oxidation is not controlled by the initial temperature, but rather by the formation and cooling of solid $Al_2O_3$ at the surface, a process that inhibits further migration of Al to the solid–air interface.

Finally, based on the analysis above, we conclude that high surface temperature, i.e. heating, not photochemistry is the critical factor in inducing this transformation. Reaching high temperatures is attributed to the effective excitation of the $Al_2O_3$ phonons, which subsequently heat the entire film. Fig. 5 shows no transformation in the pure aluminum film during laser irradiation in air because metallic aluminum absorbs little energy; its optical absorption coefficient is only 0.0431 [11], and thus the maximum surface temperature rises only to ~323 K. The self-terminating surface oxide present on the aluminum film comes mostly from ambient air oxidization at 300 K.

The tenfold increase of the RMS film roughness may arise from two sources. First, according to our calculation, the maximum surface temperature would reach ~1200 K well above the melting point of Al. At the same time the $Al_2O_3$ and the Al would expand in line with their respective thermal expansion coefficients. In this situation, molten Al would flow into any cavities that were open. When the 7 ns laser pulse terminates, the near-surface temperature drops sharply leading to solidification on a nanosecond time scale "freezing in" metastable and roughened structures. Second, in the presence of $O_2$, additional oxide will form resulting in a greater volume within the heated zone and sensibly increased roughness.

## 2.5 Summary

To summarize, 100 nm thick $Al/Al_2O_3$ cermet films, which consist of 15.5% Al and 84.5% $Al_2O_3$, were deposited by reactive sputter deposition. These cermet films were then irradiated in vacuum and air by a single 7 ns pulse from a 1064 nm laser. For a laser pulse power density of 16 MW $cm^{-2}$, the calculated maximum surface temperature after laser irradiation is ~1200 K, well above the melting point of Al. We propose that vacuum irradiation melted the aluminum, expanded the heated zone and led to increased RMS surface roughness (3.5–35.2 nm) and a re-distribution of Al and O in the outermost 35 nm of the film. Irradiation in air led not only to similar melting and roughening, but also to substantial Al oxidation. With respect to using this material in thin film form as a resist for thermal patterning, we note a concern in that the observed thermal transformation requires very high transient temperature changes.

## 2.6 References

[1] G. Pugh, J. Canning, B. Roman, IEEE custom integrated circuits conference, 149 (1998)

[2] T Brunner, IEDM, IEEE, 9 (1997)

[3] J. Canning, Int. conference on microelectronic test structures, IEEE **11**, 25 (1998)

[4] J. Melngailis, A. A. Mondelli, I. L. Berry, and R. Mohondro, J. Vac. Sci. Technol. B **16**, 927 (1998).

[5] P.C. Fazan, M. Declercq, URSI International Symposium, IEEE 128 (1998)

[6] S. W. Pang, R. R. Kunz, et al., J. Vac. Sci. Technol. B **7**, 1624 (1989)

[7] D. J. Ehrlich, J. Y. Tsao, C.O. Bozler, J. Vac. Sci. Technol. B **3**, 1 (1985)

[8] J. Melngailis, D. J. Ehrlich, S. W. Pang, J. N. Randall, J. Vac. Sci. Technol. B **5**, 379 (1987)

[9] D. Burgess, Jr., P. C. Stair, E. Weitz, J. Vac. Sci. Technol. A **4**, 1362 (1986)

[10] James E. Stewart, Optical principles and technology for engineers (Marcel Dekker Inc., 1996)

[11] David. R. Lide, et al., Handbook of chemistry and physics, 78th edition, (1997)

[12] William J. Tropf, et al., Handbook of optical constants of solid, (Academic Press, 1998)

[13] C. R.A. Catlow, et al., Mass transport in solids, (Plenum Press, 1983)

[14] G. V. Samsonov, The oxide handbook, (IFI/Plenum Press, 1973)

# Chapter 3

# *In situ* laser annealing system for real-time surface kinetic analysis

## 3.1 Introduction

X-ray Photoelectron Spectroscopy (XPS) and Ion Scattering Spectroscopy (ISS) are widely used to characterize surface and interfacial chemical reactions, epitaxial thin film growth, and atomic diffusion processes in thin films [1-3]. Typically, temperature plays a very important role in these processes and real time analysis is very desirable. This is not difficult for permanently mounted conductive samples that can be spot welded on heating leads so that the heating is very efficient and local.

However, for non-conductive samples and for systems designed for routine relatively fast sample exchange without breaking vacuum, reproducible *in-situ* heating of the sample is not trivial and is often accompanied by undesirable background pressure increases brought about by heating non-sample components. For example, as described elsewhere [4-7], we have a thin film growth and analysis facility comprised of three separate ultra-high vacuum (UHV) chambers linked together with a UHV sample transfer tube. Using this system, we annealed samples *before* inserting into the analysis chamber to perform XPS or ISS. This procedure obviously involves repeated heating and cooling thereby complicating kinetic analysis. Further, even when transferred between systems under vacuum ($< 10^{-8}$ Torr), this procedure is time consuming and can be compromised by background contamination, e.g., oxygen- and carbon-species chemisorbed.

In order to achieve real time *in-situ* surface analysis at elevated temperatures with minimal background heating effects, we have configured an XPS and ISS system with a continuous wave (CW) $CO_2$ infrared laser (~10 μm). This system works well for any sample, conducting, semi-conducting or insulating, that absorbs the 10 μm laser radiation. Compared with other methods, the high power density (up to 90 $W/cm^2$) and tight focus (0.28 $cm^2$) is a distinct advantage. Localization of the radiant energy makes it possible to minimize problems associated with species desorbing from non-sample surfaces and subsequently contaminating the surface of interest.

## 3.2 Experimental setup

A schematic diagram of the experimental system is shown in Figure 3.1. The analytical chamber consists of an X-ray photoelectron and ion scattering spectrometer (PHI 3057). A CW $CO_2$ infrared laser (Synrad series 48-2), with controllable output power between 0 and 25 W, was passed through an external beam expander to provide 0.28 $cm^2$ cross-sectional area (up to 90 $W/cm^2$). The beam was guided to the chamber with two copper mirrors and passed into vacuum through a ZnSe window. Inside the vacuum chamber, a Cu mirror mounted on a rotational feedthrough directed the laser beam through an opening in the sample manipulator toward the backside of the demountable structure on which the sample was mounted. The demountable structure is a modified PHI "puck" (see insert in Figure 3.1), of standard dimensions with a 1.5 cm dia. hole bored along its axis. Samples were clipped to the upper surface using standard Be-Cu flat springs. A thermocouple (TC1) coated with graphite was permanently inserted into the open space just beneath the sample manipulator and positioned to intercept the laser beam. A visible laser diode pointer (650 nm) was used to align the $CO_2$ laser beam pathway so that area heated from the back coincided with the face area analyzed by XPS and ISS.

For XPS, Mg Kα X-rays were used, taking spectra at a pass energy of 58 eV. The analysis area was 0.5 $mm^2$ and the acquisition time for single element

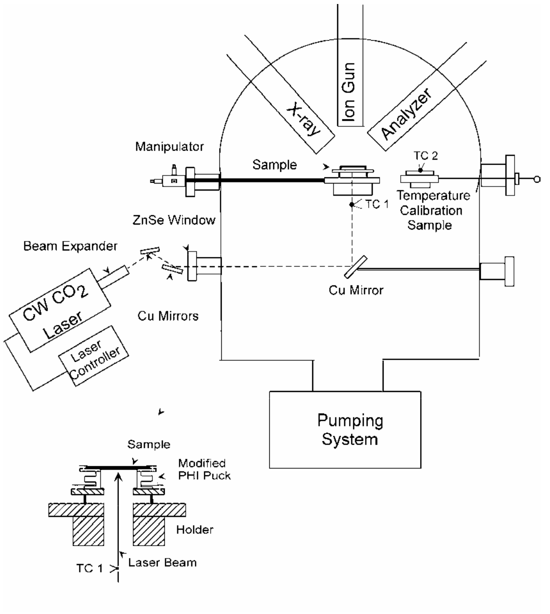

**Figure 3.1** Schematic of the XPS and ISS surface analysis system modified with a CW $CO_2$ infrared laser for *in-situ* heating of samples. The key components are external and internal copper mirrors to steer the laser beam and a ZnSe window to transmit the beam through the vacuum wall.

**Insert:** Expanded diagram of the modified PHI sample holder (puck) that is transferable between film growth and surface analysis chambers of a thin film growth and analysis facility. The key modification is the central hole through which the $CO_2$ laser beam passes to heat the sample with minimal heating of the stage on which the puck is clipped.

scan was 0.54 min. For ISS, we used 1 keV $^4$He ions and took spectra at a pass energy of 375 eV. The ISS analysis area was 3.1 mm$^2$ and the acquisition time was 1.4 min.

## 3.3 Sample preparation and temperature calibration

Because all of thin films reported in this paper were deposited on Si(100), a 2.5 × 2.5 × 0.05 cm Si(100) reference sample was used for temperature calibration. In order to enhance absorption of 10 μm radiation, the sample backside was coated with colloidal graphite (Aerodag G, Ted Pella, Inc.). A chromel-alumel thermocouple (TC2) was glued with ceramic cement to reference sample. Correlation of TC2 with TC1 provided the required calibration curve. The calibration was checked frequently; ± 5% deviations were found. In this context, it is important to note that TC1 responds much more rapidly than TC2 when the laser power is changed.

Figure 3.2 shows the sample temperature, based on TC1 readings and the calibration curve, as a function of annealing time for three different laser power densities (13, 22 and 36 W/cm$^2$). The sample temperature increased sharply to 80% of the maximum temperature in the first 5 minutes, and became stable after 20 minutes. Other measurements (not shown) indicate that temperatures as high as 800 K are reached by increasing the laser output up to 20 W (72 W/cm$^2$).

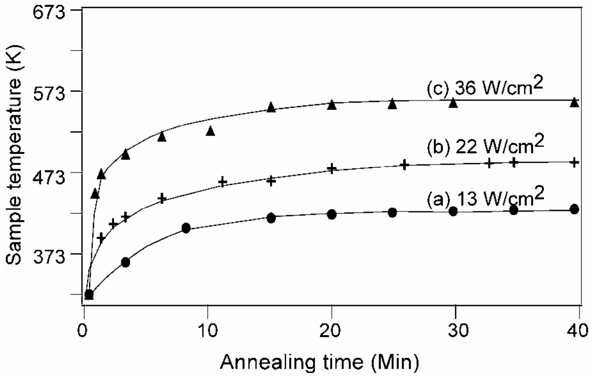

**Figure 3.2** Temperature versus time during *in-situ* vacuum annealing for laser power densities of: (a) 13, (b) 22 and (c) 36 W/cm$^2$.

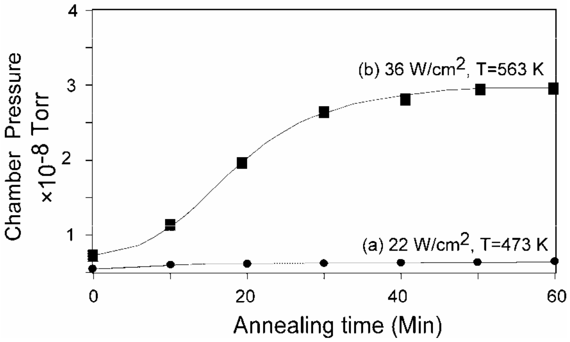

**Figure 3.3** Background pressure during *in-situ* vacuum annealing at: (a) 473 K and (b) 563 K.

Figure 3.3 shows the analysis chamber pressure change as the sample was annealed to 473 K and 563 K, respectively. The pressure was always below $1\times10^{-8}$ Torr at 473 K annealing, but rose from $6.0\times10^{-9}$ to $3.0\times10^{-8}$ Torr at 563 K after 1 hour annealing. This small pressure rise did not adversely affect the XPS or ISS measurements and minimized complications due to background gas reacting.

As a comparison, using a halogen lamp to anneal puck-mounted samples, ~ 30 W was required to reach 563 K and required ~ 40 minutes with ~ 100-fold background pressure rise. For laser annealing, only 10 W is sufficient to reach 563 K.

## 3.4 $Cu_2O$ reduction with *in-situ* vacuum annealing at 563 K

As a test case, we studied the surface reduction kinetics of an oxidized Cu surface. The samples comprised air oxidized ~700 nm thick Cu films deposited on Si (100). The reduction process is generally described as two steps: first, the CuO is reduced to $Cu_2O$; second, $Cu_2O$ is reduced to Cu metal [8-9]. Here we only address the kinetics of the second step.

Real time XPS high resolution scans were carried out while the Cu film with surface $Cu_2O$ was annealed using the laser power density of 36 $W/cm^2$ (563 K is reached). Over a 25 min span, Figure 3.4 shows Cu LMM Auger (a) and O 1s (b) intensities collected at various times and temperatures with $t = 0$ arbitrarily set when T reached 463 K. This figure clearly reveals the

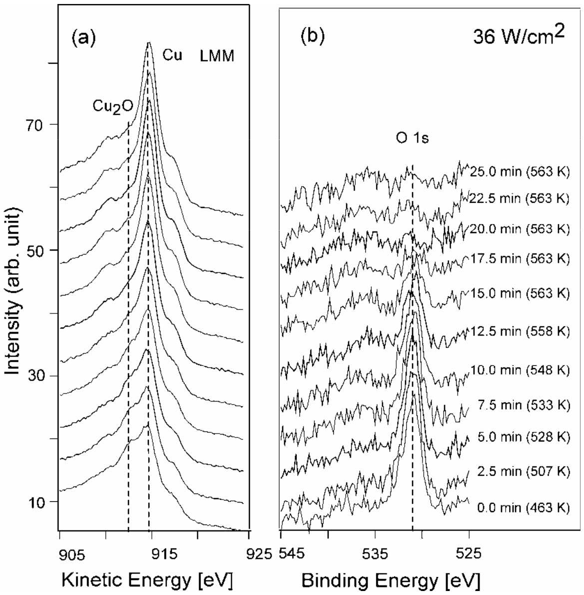

**Figure 3.4** For a $Cu_2O$/Cu film, high resolution XPS spectra during *in-situ* vacuum annealing for a laser power of 10 W focused to 0.28 $cm^2$ (36 $W/cm^2$): (a) Cu LMM Auger and (b) O 1s intensities. The annealing times and temperatures are given for each curve.

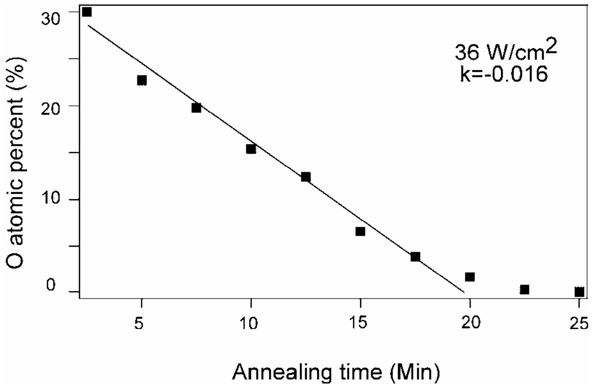

**Figure 3.5** Calculated from oxygen and copper XPS signals of Figure 3.4, the atom % O during *in-s*itu vacuum annealing for laser power density of 36 W/cm$^2$ (T=563 K, see Figure 3.4). The effective rate coefficient calculated from the slope of this line is – 0.016 atom %/min.

kinetics of $Cu_2O$ reduction. At t = 0, there was a broad Cu LMM peak with a significant shoulder at ~2 eV lower kinetic energy than Cu metallic peak. This shoulder, characteristic of $Cu_2O$, decreased gradually and disappeared at ~ 20 minutes. Correspondingly, the surface O 1s peak decayed and vanished over the same time interval.

The atomic percent oxygen, calculated as a function of annealing time (Figure 3.5), decayed linearly with time, i.e., a zero order reduction process. From the slope, the rate coefficient is k = 0.016 atom %/min.

Companion ISS data, Figure 3.6, reflects changes in the exposed Cu during annealing.  Prior to vacuum annealing, only a weak Cu peak was identified (not shown). When reaching 463 K (t = 0), Cu was easily detected and increased linearly by one order of magnitude up to 20 min. when it stabilized (Figure 3.7). The order of magnitude increase of Cu ISS signal is attributed to two factors: removal of surface carbon and oxygen atoms and reduction of Cu oxide to metallic Cu. The insert of Figure 3.6, shows XPS C 1s spectra corresponding bottom to top of the ISS spectra. Although XPS probes much deeper than ISS, this spectra shows surface carbon was removed gradually during annealing.

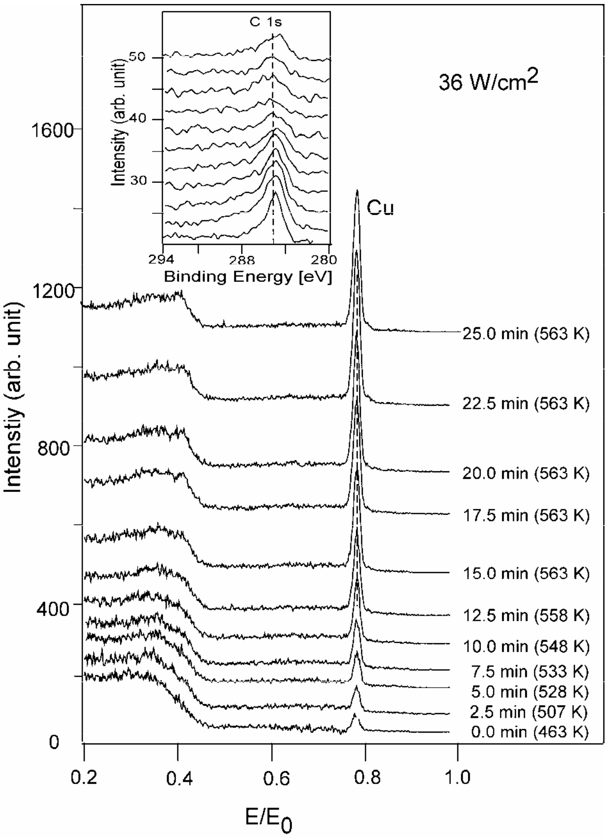

**Figure 3.6** For a $Cu_2O$/Cu film, ISS measured during *in-situ* vacuum annealing for a laser power of 10 W focused to 0.28 $cm^2$ (36 W/$cm^2$). Times and temperatures are given on each curve. The corresponding C 1s spectra are shown in the insert (stacked in the same way as ISS).

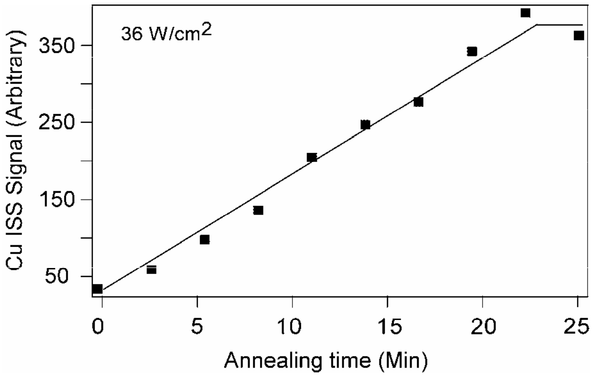

**Figure 3.7** Cu ISS peak height during *in-situ* vacuum annealing for laser power density of 36 W/cm$^2$. (T=563 K, see Figure 3.6).

## 3.5 Summary

An XPS and ISS surface analysis instrument has been modified for vacuum annealing using a continuous wave $CO_2$ infrared laser The capability is illustrated by using real time XPS and ISS to measure the reduction kinetics of a thin copper oxide ($Cu_2O$) film.

## 3.6 References

[1] D. Briggs and M. P. Seah, Practical surface analysis, 2nd ed., Vol. 1, 2 (Wiley, London, 1992).

[2] J. I. B. Wilson, J. S. Walton and G. Beamson, J. Electron Spectrosc. Relat. Phenom., **121**, 183 (2001).

[3] M. Matsui, T. Tatsumi and M. Sekine, J. Vac. Sci. Technol. A **19**, 1 (2001).

[4] Y.-M. Sun, S. Y. Lee, A. Lemonds, J. Lozano, J.-P. Zhou, J. G. Ekerdt, J. M. White and I. Imesh, Surf. Interface Anal., **32**, 79 (2001)

[5] Y.-M. Sun, S. Y. Lee, E. R. Engbrecht, K. Pfeifer, S. Smith, J. M. White and J. G. Ekerdt, Mater. Res. Soc. Symp. Proc. **648,** P6.43 (2001)

[6] Y.-M. Sun, S. Y. Lee, A. M. Lemonds, E. R. Engbrecht, S. Veldman, J. Lozano, J. M. White, J. G. Ekerdt, I. Emesh and K. Pfeifer, Thin Solid Films **397**, 109 (2001)

[7] S.Y. Lee, N. Mettlach, N. Nguyen, Y.-M. Sun and J.M. White, Appl. Surf. Sci. (submitted) (2002).

[8] S. Poulston, P. M. Parlett, P. Stone and M. Bowker, Surf. Interface Anal., **24** 811 (1996).

[9] Y. Z. Hu, R. Sharangpani and S.-P. Tay, J. Electrochem. Soc. **148**, G669 (2001).

# Chapter 4

# Low-temperature chemical vapor deposition of ruthenium films on tantalum

## 4.1 Introduction

In the current copper (Cu) interconnect technology (130 nm node), tantalum (Ta) and tantalum nitride (TaN) are deposited on an interlayer dielectric as Cu diffusion barriers, followed by deposition of a Cu seed layer to enable the subsequent Cu electroplating. Currently, physical vapor deposition (PVD) is the dominant technology to form this Ta/TaN/Cu seed multilayer stack, and it may be extendable to the 65 nm node technology [1]. However, as integrated circuit devices scale down to the 45 nm generation (in 2010) and beyond, deposition of an ultra-thin, conformal, continuous barrier/seed bi-layer (<5 nm) in a very high aspect ratio trench/via hole, to which PVD may not extend, will be required. Thus, the development of new ultrathin barrier materials and chemical deposition pathways is motivated. One approach for the 45 nm node technology and beyond, could employ a thin layer of Ta as the primary barrier covered by a thin layer of ruthenium (Ru) to improve adhesion of an overlayer of Cu, and to allow direct electroplating of Cu on the barrier without Cu seed layer deposition.

Ru is a noble metal with a low electrical resistivity (7.6 μΩ·cm) [2], approximately half that of Ta. The insolubility of Ru with Cu [3] is an especially favorable attribute for a barrier material. Metallic Ru is the stable physical state in the acid solutions used in Cu electroplating [4], and successful Cu electroplating on Ru was recently reported [5].

Previous studies of the metallorganic chemical vapor deposition (CVD) of Ru films have utilized several precursors: $Ru(Cp)_2$ (Cp, cyclopentadienyl), $Ru(acac)_3$ derivatives (acac, acetylacetonate) [6], $Ru(EtCp)_2$ (EtCp, ethylcycloentadienyl) [7], and $Ru(OD)_3$ (OD, 2,4-octanedionate) [8]. Typically, these precursors require temperatures in excess of 673 K to facilitate ligands removal or oxygen to combust organic ligands to form Ru or $RuO_2$ films. This approach is not applicable when the substrate is oxygen sensitive, as is the case with Ta. In this paper, we report on the low temperature CVD of Ru films on Ta and $SiO_2$ using ruthenium carbonyl [$Ru_3(CO)_{12}$]. $Ru_3(CO)_{12}$ has labile CO leaving groups, and thermally decomposes without any reactive gas at relatively low temperatures [3,9]. Film properties were characterized by X-ray photoelectron spectroscopy (XPS) and low energy ion scattering spectroscopy (ISS). In this chapter we report: (1) growth of Ru films using CVD at temperatures as low as 423 K and (2) full coverage of Ta by such a thin Ru film (2.5 nm), as calculated by combining ISS data with XPS Ta 4f peak attenuation.

## 4.2 Experimental

A 150 nm-thick Ta substrate was first deposited at 300 K on a Si wafer using PVD. A Ta target was sputtered 15 min using 20 standard cubic centimeters per min (sccm) Ar gas, which was directly injected into the sputter gun operating at 100 W DC power. The chamber pressure during film growth was maintained at 10 mTorr. A 500 nm-thick $SiO_2$ substrate on a Si wafer was obtained from International Sematech.

The Ru film growth and subsequent XPS and ISS analysis were carried out in a film deposition and analysis facility consisting of a vacuum sample transfer system, load lock, analysis, PVD and CVD chambers [10]. The Ru carbonyl was sublimed at 366 K to obtain sufficient vapor pressure and delivered to the CVD chamber using 10 sccm Ar through a heated gas line and shower head. The deposition was carried out at 50 mTorr and the substrate was heated between 423 and 593 K.

## 4.3 Results and Discussion

XPS of a 6 nm Ru film grown at 423 K on Ta (Figure 4.1) shows, as expected, negligible oxygen incorporation (right side), a Ru 3d region characteristic of unoxidized Ru and, accounting for the C 1s-Ru 3d overlap, very little ($\leq$ 1%) carbon. Here the A broad scan (not shown) has no peak attributable

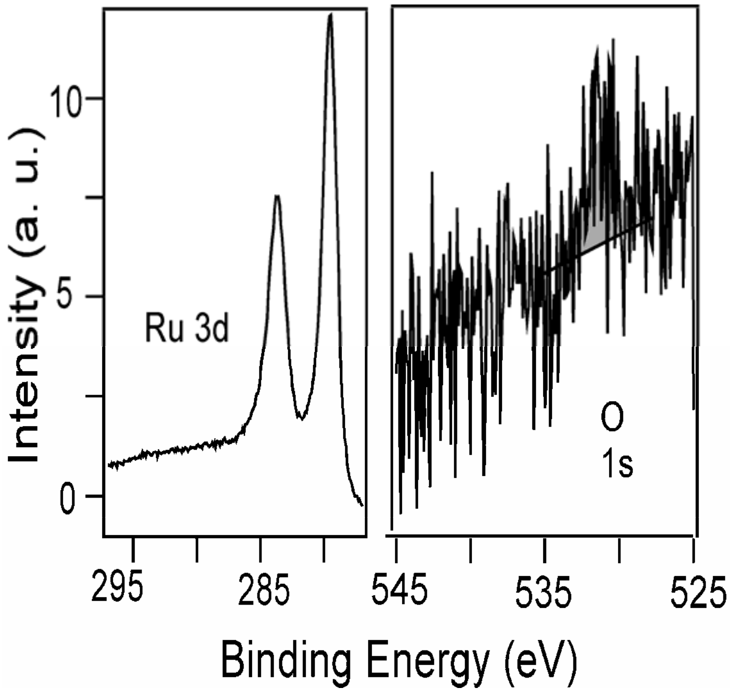

**Figure 4.1** Ru 3d (left) and O 1s (right) XPS of a 6 nm Ru film grown at 423 K on Ta by CVD using $Ru_3(CO)_{12}$.

to the underlying Ta film. The Ru films were relatively smooth; measured by AFM (not shown), the rms roughnesses of the initial Ta and 6 nm Ru-on-Ta film were 0.7 and 1.2 nm, respectively. Measured using a four-point probe, a very thin (3.5 nm) Ru film grown on a $SiO_2$ substrate has low electrical resistivity of 30 $\mu\Omega\bullet$cm compared to bulk Ru (7.6 $\mu\Omega\bullet$cm). Pure Ru films were also grown on Ta at 493 and 593 K, respectively. Thus, we conclude that, without adding any co-reactant, $Ru_3(CO)_{12}$ decomposes to form metallic Ru at temperatures as low as 423 K.

To establish the minimum amount of Ru needed to form a continuous film over the Ta substrate, ISS was measured (Figure 4.2) for average Ru film thicknesses of: 0, 1.6, and 2.5 nm, calculated by XPS Ta 4f peak attenuation. The Ta ISS signal drops below the detection limit at some point between 1.6 and 2.5 nm Ru. To assess thermal stability, a 3 nm Ru film was annealed in vacuum at 573 K for 40 min and examined by XPS measurements (not shown), which show negligible changes. We conclude that neither inter-diffusion nor Ru de-wetting occurs. Clearly, the Ru/Ta interface is thermally stable.

Figure 4.3 (a) shows XPS Ta 4f spectra of a 150 nm Ta film deposited by sputtering on Si (100), characteristic of metallic Ta with slight oxidization on the surface. When this Ta film was exposed to air for 30 minutes and then measured with XPS (Figure 4.3 (b)), two new Ta 4f peaks appeared at the binding energy of 26.1 and 28.0 eV, characteristic of fully oxidized Ta.

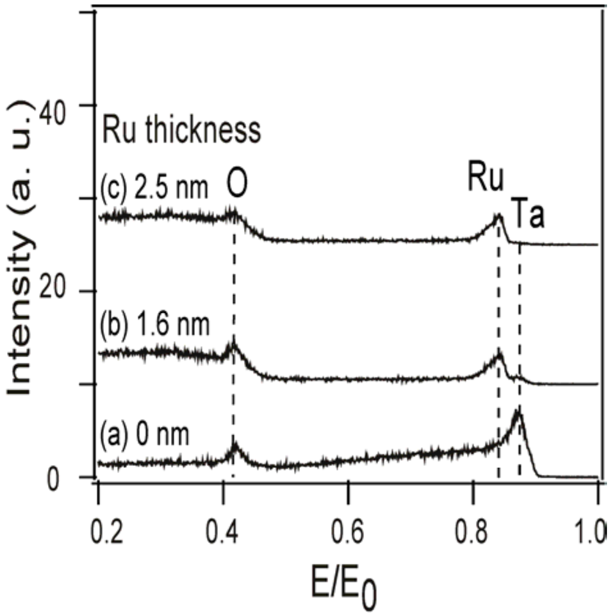

**Figure 4.2** ISS of Ru films grown at 423 K. The spatially averaged Ru thicknesses are: (a) 0 nm, (b) 1.6 nm, and (c) 2.5 nm. It is very important to note that smooth Ru films were assumed.

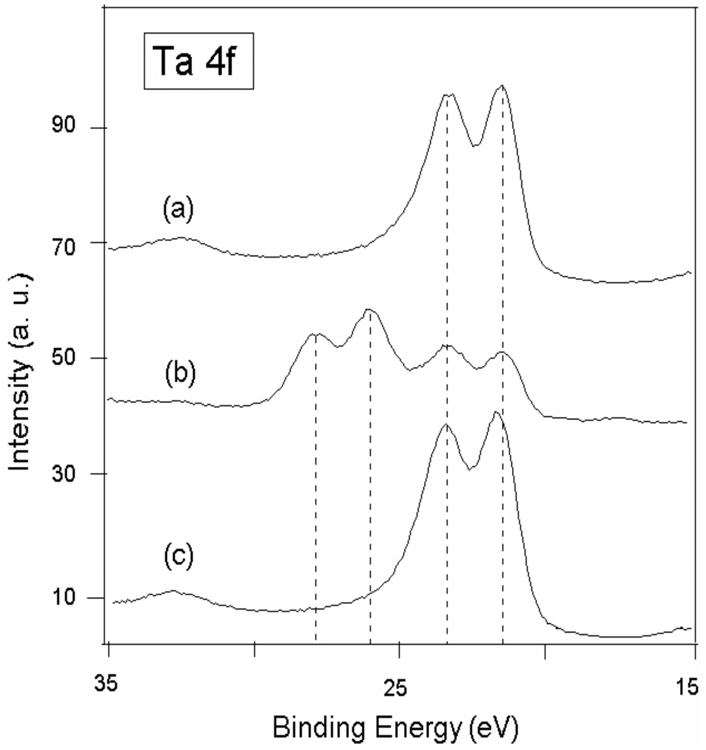

**Figure 4.3** Ta 4f XPS of (a) an as-grown PVD Ta film; (b) after exposure the Ta film to air 30 min; and (c) after exposure Ru(6 nm)/Ta bi-layer film to air 30 min. and followed by 5 kV Ar sputtering to remove top Ru layer.

Obviously, Ta is very easily oxidized in air, which results in the formation of an insulating oxide layer. Moreover, our XPS results (not shown) illustrated that the PVD Ta film was so oxygen/moisture sensitive that its surface was oxidized even during high vacuum ($10^{-7}$ Torr) annealing. However, when a 6 nm Ru film was deposited *in-situ* on the top of the Ta film and the resulting composite Ru/Ta film was then exposed to air for 30 minutes, XPS of the Ta film (Figure 4.3 (c)), after removing the top Ru layer using 5 kV Ar sputtering, yielded a congruent spectra as that of the as-deposited Ta film. This result indicates that a 6 nm Ru film can effectively prevent oxidation of Ta in air. Also, the Ru film can prevent Ta oxidation during high vacuum annealing. Although the Ru film surface was slightly oxidized in air, it is essential to note that the ruthenium dioxide, unlike tantalum oxide, is still conductive (40 $\mu\Omega\cdot$ cm) [2]. Therefore, compared with Ta film only, the composite Ru/Ta films have excellent resistance to oxidization so as to ensure a low barrier film resistivity, a critical factor for improving speed of micro-devices.

Figure 4.4 shows ISS and XPS (insert) results for a 3.5 nm CVD Ru film before (a) and after (b) deposition, by PVD, of a 0.3 nm (~2 ML) Cu film. The Cu thickness is based on attenuation of the Ru 3d intensity. Comparing (a) and (b) shows that the Ru signal is completely suppressed, implying that 0.3 nm of Cu is sufficient to fully cover the Ru. A ten-fold larger amount of Cu (3.5 nm) is required to fully cover a Ta film (not shown).

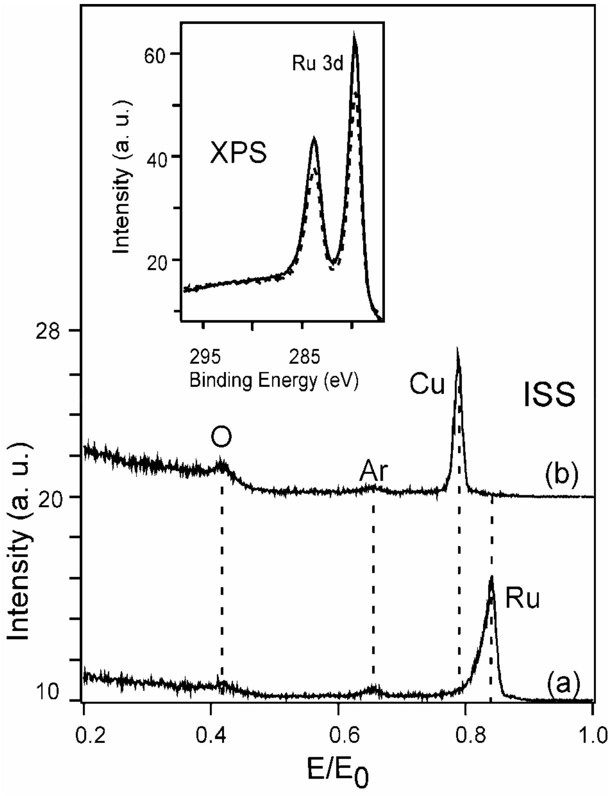

**Figure 4.4** ISS of (a) an as-grown Ru film on Ta and (b) a 0.3 nm Cu film grown on Ru. The insert is the Ru 3d XPS of an as-grown Ru film (solid line), and after 0.3 nm Cu film deposition (dashed line).

It is important to note that the ISS data always exhibit features assigned to oxygen. From XPS data (not shown) the Ta film was slightly oxidized, whereas the O 1s intensity for the Ru film (Figure 4.1) is at the detection limit. This oxygen may inhibit Cu wetting on Ta [11] but not Ru. Combining XPS and ISS, we conclude that this oxygen is localized on the Ru surface and that a small amount of oxygen is adsorbed from the background of the sample preparation and transfer vacuum chambers. In addition, the Ar signals in Figure 4.3 were attributed to background contamination in the XPS ion gun since both He and Ar were used.

From the foregoing results, several attractive features of $Ru_3(CO)_{12}$ emerge. First, no co-dosed gas, e.g., $O_2$, is needed to grow Ru films using this precursor. Thus, without risk of oxidizing an underlying metal, Ru can be grown over, for example, Cu and Ta. As a result, the underlying metal properties are not compromised by adding Ru.

Second, film deposition using $Ru_3(CO)_{12}$ is realized with a relatively low thermal budget; films grow at temperatures as low as 423 K (150 $^oC$), a temperature at least 50 $^oC$ lower than reported for other Ru precursors [4-6]. This lower temperature of decomposition is particularly important when considering nucleation of Ru at the surface of a second material, e.g., Ta and $SiO_2$. As the surface temperature is lowered, the residence time of molecular $Ru_3(CO)_{12}$ increases. Since the activation energy for partial dissociation (leading to nucleation) is readily met, this makes desorption compete less effectively with dissociation. Consequently, as compared to situations where dissociation probabilities are very small, there is a relatively short induction time, many Ru particles are nucleated, and a smooth Ru film grows on this high density of nucleated centers.

Third, the excellent Cu wettablity on Ru, evidenced by the results summarized above, reveals that the initial Cu adatoms make stronger bonds with underlying Ru compared to Cu-Cu atom interactions. Thus, a strong adhesion property between Cu and Ru can be reasonably predicted.

Finally, attention is drawn to the valuable insight provided by the combination of XPS and ISS. Because the scattering of low energy ions is uniquely surface sensitive, it determines, for deposition of an adlayer on a substrate, when the substrate is fully covered. At this point, XPS provides the average thickness of the overlayer. In this way, we determined that 2.5 nm of Ru is sufficient to cover a Ta substrate and that 0.3 nm of Cu completely covers Ru. It is well to keep in mind that ISS peak positions vary weakly with atom mass. As a result, typically, for application of ISS, the metals must be, as here, from different rows of the periodic table.

## 4.4 Summary

In summary, pure, smooth and uniform Ru films on Ta and low resistivity films on $SiO_2$ were grown by thermal CVD at temperatures as low as 423 K (150 $^oC$) using $Ru_3(CO)_{12}$. Measured using XPS and ISS and assuming smooth films, a 2.5 nm Ru film fully covers underlying Ta, and the Ru/Ta interface is thermally stable up to at least 573 K. The composite Ru/Ta film proved to have an excellent resistance to oxidization under high vacuum annealing as well as exposure to ambient air. In contrast to Ta, the Ru film exhibits excellent wettability by Cu even when the Ru surface is contaminated with small amounts of oxygen.

## 4.5 References

[1] International Technology Roadmap for Semiconductors, 2001 edition, http://pubic.itrs.net/ (2001)

[2] J. Emsley, The Elements, 3rd ed. (Oxford, 1998)

[3] T. B. Massalski, Editor, Binary Alloy Phase Diagram, 2nd ed. (Materials Information Society, Material Park, OH, 1990).

[4] M. Pourbaix, Atlas of Electrochemical Equilibria in Aqueous Solutions, 1st ed. (Oxford, 1966).

[5] Chyan, T. N. Arunagiri, and T. Ponnuswamy, J. Electrochem. Soc. **150**, C347 (2003).

[6] M. L. Green, M. E. Gross, L. E. Papa, K. J. Schnoes, and D. Brasen, J. Electrochem. Soc. **132**, 2677 (1985).

[7] Y. Matsui, M. Hiratani, T. Nabatame, Y. Shimamoto, and S. Kimura, Electrochem. Solid-State Lett. **4**, C9 (2001).

[8] J.-H. Lee, J.-Y. Kim, S.-W. Rhee, D.-Y. Yang, D.-H. Kim, C.-H. Yang, Y.-K. Han, and C.-J. Hwang, J. Vac. Sci. Technol. A **18**, 2400 (2000).

[9] E. P. Boyd, D. R. Ketchum, H. Deng, and S. G. Shore, Chem. Mater. **9**, 1154 (1997).

[10] Y.-M. Sun, S. Y. Lee, A. M. Lemonds, E. R. Engbrecht, S. Veldman, J. Lozano, J. M. White, J. G. Ekerdt, I. Emesh and K. Pfeifer, Thin Solid Films **397**, 109 (2001).

[11] L. Chen, N. Magtoto, B. Ekstrom, and J. Kelber, Thin Solid Films **376**, 115 (2000).

# Chapter 5

# Low temperature chemical vapor deposition of ruthenium films on silicon dioxide

## 5.1 Introduction

Ruthenium (Ru) is a noble metal and has been investigated as a candidate material for future generation capacitor electrodes in memory applications such as gigabit DRAMs and FRAMs devices due to its low resistivity (7.6 μΩ·cm) [1], high chemical inertness, and good thermal stability [2-4]. Recently, significant attention has been drawn to Ru for its newfound application as a potential copper (Cu) diffusion barrier, a promising advance for future 45 nm node ultra-large scale integrated circuit (ULSI) interconnects and beyond [5-7].

Compared with the current barrier material of Tantalum (Ta)/Tantalum nitride (TaN), Ru only has half the resistivity of Ta, and is not as easily oxidized. Its supreme conductivity and insolubility with Cu [8] provide Ru with the essential factors to serve as a good barrier material for future ULSI processes. More attractively, it has been proven that Cu can directly electroplate on the Ru surface [7]. As a result, it may make unnecessary the step of PVD Cu seed layer deposition, substantially simplifying the back-end of line (BEOL) process.

We have reported a low-temperature CVD process to grow a pure, smooth and uniform Ru film on Ta substrate using ruthenium carbonyl ($Ru_3(CO)_{12}$) precursor [5]. Compared with other metal-organic precursors such as $Ru(acac)_3$ derivatives (acac, acetylacetonate) [9] $Ru(Cp)_2$ (Cp, cyclopentadienyl) [9-11], $Ru(OD)_3$ (OD, 2,4-octanedionate) [12], and $Ru(EtCp)_2$ (EtCp, ethylcycloentadienyl) [13-15], $Ru_3(CO)_{12}$ required a deposition temperature at least 50 $^{o}$C lower than that reported for any other Ru precursors. More importantly, no co-dosed gases (e. g. oxygen) were needed in our Ru CVD process, which avoided compromising the properties of the underlying metal, Ta or Cu, in the process of adding Ru.

As a copper diffusion barrier, the barrier film typically deposits on the inter-layer dielectrics, which currently consist of a $SiO_2$ base material. In this chapter we report CVD Ru deposition on blank $SiO_2$ and patterned $SiO_2$ using the $Ru_3(CO)_{12}$ precursor. Film properties were characterized by x-ray photoelectron spectroscopy (XPS), low energy ion scattering spectroscopy (ISS), scanning electron microscopy (SEM), and X-ray diffraction (XRD).

The capacitance vs. voltage (C-V) test of a MOS capacitor with a structure of Cu/diffusion barrier/$SiO_2$/Si has been used to evaluate barrier properties of different barrier materials [16-20]. The shift of the capacitor C-V curve to the negative direction after thermal annealing would indicate penetration of Cu through the barrier layer into $SiO_2$. Compared with physical depth profiling techniques like SIMS, XPS and AES, this electrical measurement method has been shown to be much more sensitive to detect barrier failure [21]. In this chapter, we used this C-V test to evaluate the barrier properties of CVD Ru and composite Ru/Ta films.

## 5.2 Experimental

The film growth and subsequent surface analysis and electrical measurements were carried out in a film deposition and characterization facility, consisting of a load lock chamber, sample transfer system, surface analysis chamber, electrical test chamber, PVD chamber and CVD chamber [22].

Ruthenium films were deposited in the CVD chamber with a base pressure of $5\times10^{-8}$ Torr. Ruthenium carbonyl precursor, $Ru_3(CO)_{12}$ (purity 99.99%, Strem Chemicals), which was loaded in a metal-glass bubbler, was heated to 366 K. Using 10 sccm Ar carrier gas, the evaporated precursor was delivered into the CVD chamber through a gas line and shower head, both of which were heated 10 K higher than the bubbler temperature to avoid precursor condensation. The substrate was heated between 423 K and 593 K, and the chamber pressure was maintained at 50 mTorr during film deposition.

Two blank $SiO_2$ wafers with thicknesses of 500 nm and 15 nm, and a patterned $SiO_2$ trench wafer with minimum feature size of 0.17 μm were obtained from International Sematech.

The film composition was analyzed using a PHI 3057 X-ray photoelectron spectrometer. For XPS analysis, Mg $K\alpha$ X-rays were operated at pass energies of 117.4 eV for surveys and 58.7 eV for high-resolution scans. In order to obtain a depth profile or to remove surface contamination, some films were sputtered with 5 kV Ar ions at a sample current of 1 μA.

The film surface morphology and step coverage properties were measured using a LEO 1530 SEM. The film microstructure was measured using a Bruker-Nonius D8 advance θ-2θ XRD.

For barrier C-V tests, Cu/Ru and Cu/Ru/Ta dots were deposited on a 15 nm gate quality $SiO_2$ on p-type Si using a shadow mask with 500 nm diameter holes. First, the Ru dots were deposited using the same CVD Ru process described above. For the electric testing of composite Ru/Ta barriers, 0.6 nm thick PVD Ta dots were first sputter deposited using 10 sccm Ar at 10 W DC power, followed by CVD Ru deposition. Second, 350 nm PVD Cu dots were *in-situ* deposited on the top of the Ru dots using the same shadow mask. In order to minimize damage of energetic sputtered Cu atoms to the devices, a 2-step Cu PVD deposition process was applied: the Cu target was first sputtered 20 minutes using 10 sccm Ar at a 10 W DC power. The total chamber pressure was maintained at 10 m Torr. Subsequently, the DC power was increased to 50 W for an additional 30 minutes of deposition to grow thick Cu dots, which ensure a good electric contact with the measurement tip. The sample substrate backside was metallized with sputtering deposited Al after scratching through the thin oxide. Finally, the as-deposited test structures were *in-situ* annealed at 623 K for 90 minutes to completely neutralize interface trapped charge.

A C-V curve of the as-grown test sample was measured using a Keithley 590 CV analyzer and an S4200 semiconductor characterization system. The voltage swept from –5 V to +5 V at a step of 0.2 V/S. The measurement frequency was 1 MHz. The sample was then annealed 60 minutes in a quartz tube oven at 623 K while flowing 10 sccm $H_2$(10%)/$N_2$ forming gas. A C-V curve of the annealed sample was collected using the same measurement conditions above.

## 5.3 Results and discussion

### 5.3.1 Ru deposition on blank $SiO_2$

Figure 5.1 shows XPS of a CVD Ru film deposited on 500 nm thick $SiO_2$ at 458 K. The O 1s spectra (right side) shows that there was little oxygen (~4%) incorporated in the film. The binding energy of the Ru 3d peak (left side) indicates that the as-deposited film was a metallic Ru film. In the presence of Ru, it is difficult to directly measure carbon content by XPS since the C 1s peak overlaps with the Ru $3d_{3/2}$ peak. However we quantitated the C

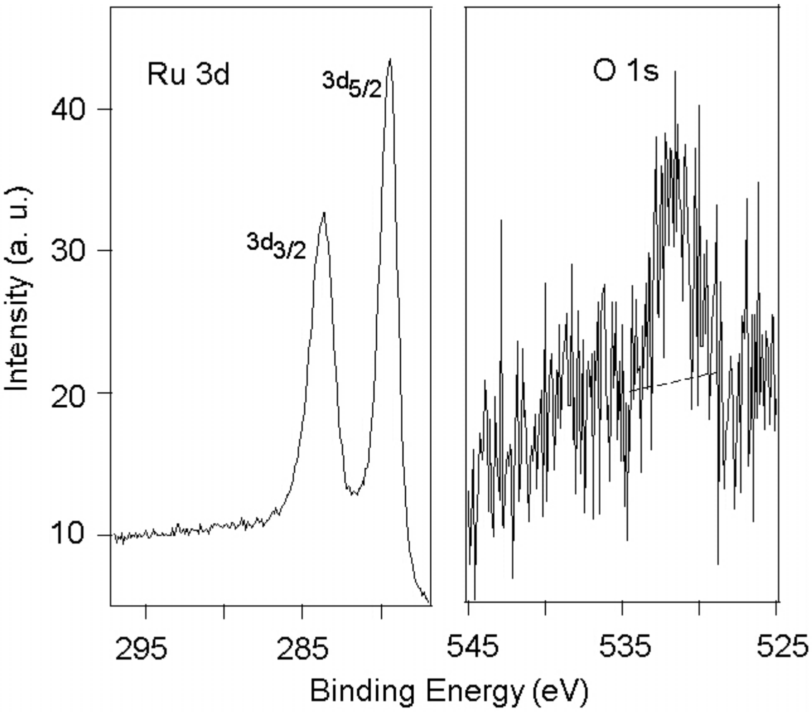

**Figure 5.1** Ru 3*d* (left) and O 1*s* (right) XPS of a CVD Ru film deposited at 458 K on $SiO_2$ by CVD using $Ru_3(CO)_{12}$.

content by calculating the peak ratio of the two Ru 3d peaks and the result revealed that there was very little carbon (<1%) contained in the Ru film.

A planar view SEM image of a Ru film (Figure 5.2) showed a uniform film surface with a particle size of ~10 nm. The X-ray diffraction pattern of a 600 nm thick Ru film grown on $SiO_2$ (Figure 5.3) shows that the film was polycrystalline with three orientation planes of (100), (002) and (101). Comparing these three XRD peaks revealed that the film was not randomly oriented, but it preferred to grow along the (100) plane.

Low energy ISS was taken (Figure 5.4) for the average Ru film thicknesses of: 0, 1.7, 2.0 and 2.5 nm, calculated by XPS Si 2p peak attenuation. The Si ISS signal drops below the detection limit at some point between 2.0 and 2.5 nm Ru. Because low energy ISS can only detect the chemical compositions of the topmost monolayer, the ISS results indicate the minimum thickness of a continuous CVD Ru film on the $SiO_2$ substrate is around 2.0 – 2.5 nm. Moreover, the discontinuous features for Ru film thicknesses of 1.7 and 2.0 nm reveal that there is a three-dimensional island growth mode during the initial Ru film deposition process.

To assess thermal stability, a 2.5 nm Ru film grown on a 15 nm thick $SiO_2$ substrate was annealed in vacuum at 673 K for 1 hr and examined *in-situ* by XPS measurements (not shown), which disclosed negligible changes. We conclude that neither interdiffusion nor Ru de-wetting occurred. It is clear that

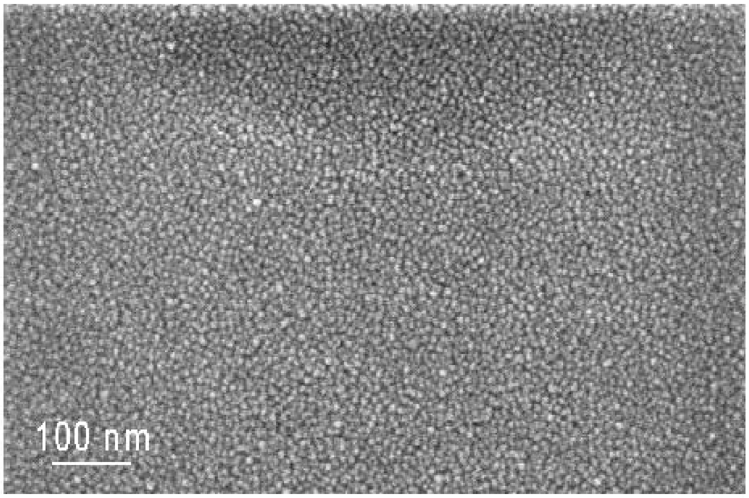

**Figure 5.2** SEM of a CVD Ru film deposited at 423 K on $SiO_2$.

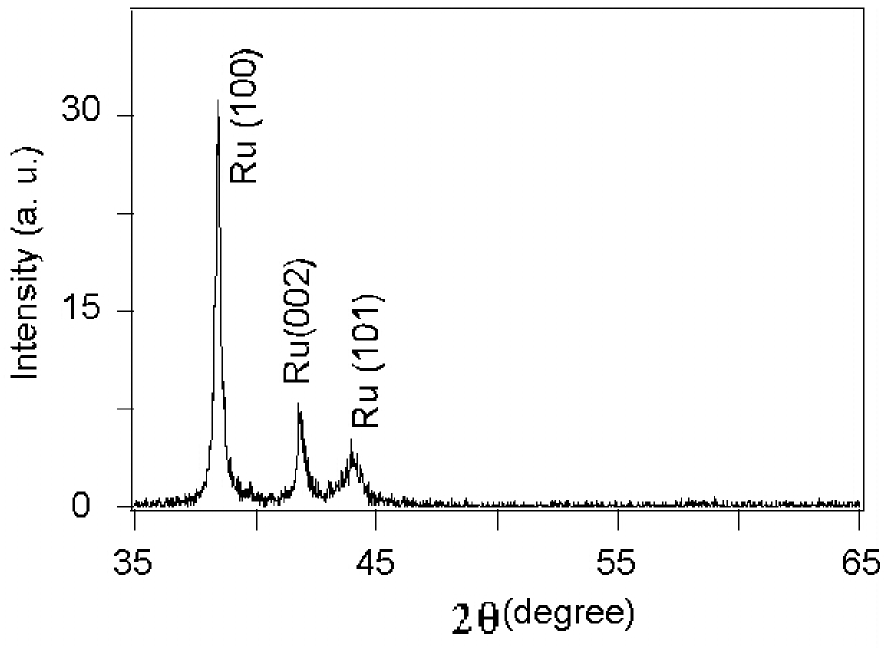

**Figure 5.3** XRD of a 600 nm Ru film deposited at 458 K on $SiO_2$.

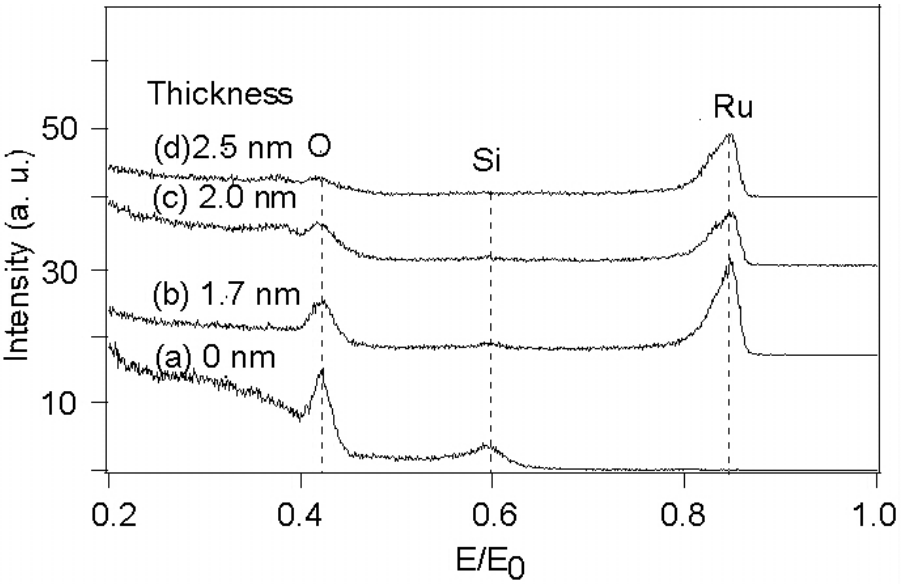

**Figure 5.4** ISS of Ru films deposited at 423 K. The spatially averaged Ru thicknesses are (a) 0 nm, (b) 1.7 nm, (c)2.0 nm and (d) 2.5 nm. It is very important to note that smooth Ru films were assumed.

the Ru/$SiO_2$ interface is thermally stable. In order to investigate Ru adhesion, a 3 nm thick Ru film was deposited on 15 nm $SiO_2$ substrate, followed by 500 nm PVD Cu deposition. This Cu/Ru/$SiO_2$ multilayer structure passed the Scotch$^{TM}$ tape test which revealed excellent interfacial adhesion properties between Cu and Ru as well as between Ru and $SiO_2$.

### 5.3.2 Ru deposition on patterned $SiO_2$

In order to investigate film step-coverage, a 600 nm thick Ru film was deposited at 458 K on a 600 nm wide $SiO_2$ trench sample with a 2:1 aspect-ratio. The SEM image (Figure 5.5) shows the Ru film covering all of the trench bottom and sidewalls. The film thickness, however, on the sidewalls and bottom of the trench appear much thinner than that of the film on the top surface, thus the percent conformity, defined as $(d_{\min}/d_{\max})*100\%$, was calculated as only 25%. Here $d_{\max}$ and $d_{\min}$ are the film thicknesses at the top surface and at the bottom of the sidewall surface, respectively (shown in Figure 5.5).

The poor conformity growth may be attributed to a relatively high reactive sticking coefficient of the $Ru_3(CO)_{12}$ precursor. Because Ru films can grow at temperatures as low as 423 K (150 $^{o}$C), [5] the activation energy for precursor dissociation was readily met at our film growth temperature of 458K. This makes the decomposition of adsorbed $Ru_3(CO)_{12}$ molecules compete more effectively with desorption of the precursor from the surface. Therefore,

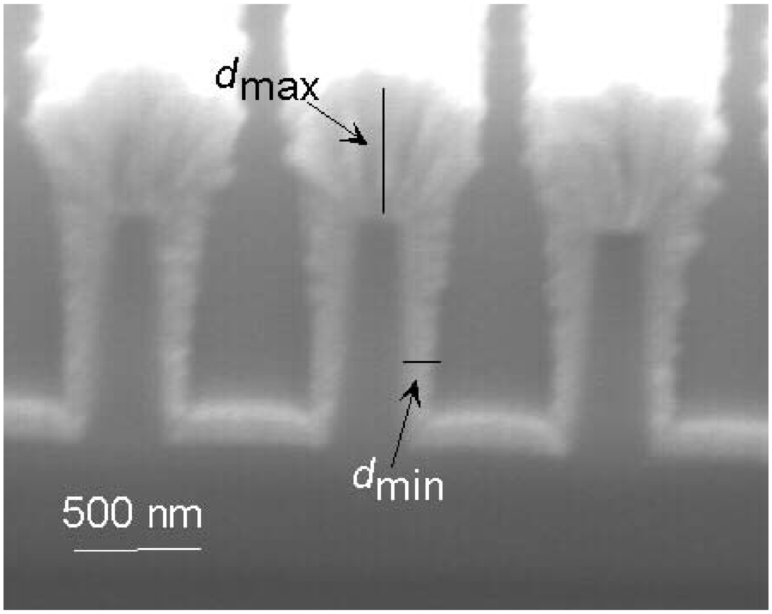

**Figure 5.5** SEM of a 600 nm Ru film deposited at 458 K on a 600 nm wide $SiO_2$ trench with a 2:1 aspect ratio

most of precursors directly decomposed and formed Ru on the top surface while very few precursor molecules had a chance to migrate into the bottom and sidewalls of the trench. Consequently, a thick film was formed on the top of the trench and a much thinner film of Ru was grown on the sidewalls and bottom of the trench.

### 5.3.3 Diffusion barrier properties of Ru and composite Ru/Ta films

The copper diffusion barrier properties of Ru and composite Ru/Ta films were characterized using C-V tests with Cu/Barrier/$SiO_2$/Si capacitors. First, a 2.5 nm and a 4 nm thick Ru films were prepared and then annealed at 623 K for 60 minutes in $H_2$ (10%)/$N_2$ ambient. Compared with the C-V curve before annealing (curve (a) in Figure 5.6), the post-annealing C-V curve of the 2.5 nm Ru film (curve (c) in Figure5.6) shifted to the negative side. However, there is not any change of the C-V curve for the 4 nm Ru film (curve (b) in Figure 5.6). Therefore, a 4 nm thick CVD Ru film can effectively prevent Cu diffusing into thermal oxide under our test conditions, but a Ru film as thin as 2.5 nm cannot form a good diffusion barrier. As mentioned earlier in this chapter, our CVD Ru film growth was a 3-D island growth process, and 2.5 nm is approximately the minimum thickness to form a continuous film on $SiO_{2,}$ based on XPS and ISS measurements. Thus, it is reasonable to expect the structure of this 2.5 nm Ru film is still very loose and has many defects, through which Cu can easily penetrate.

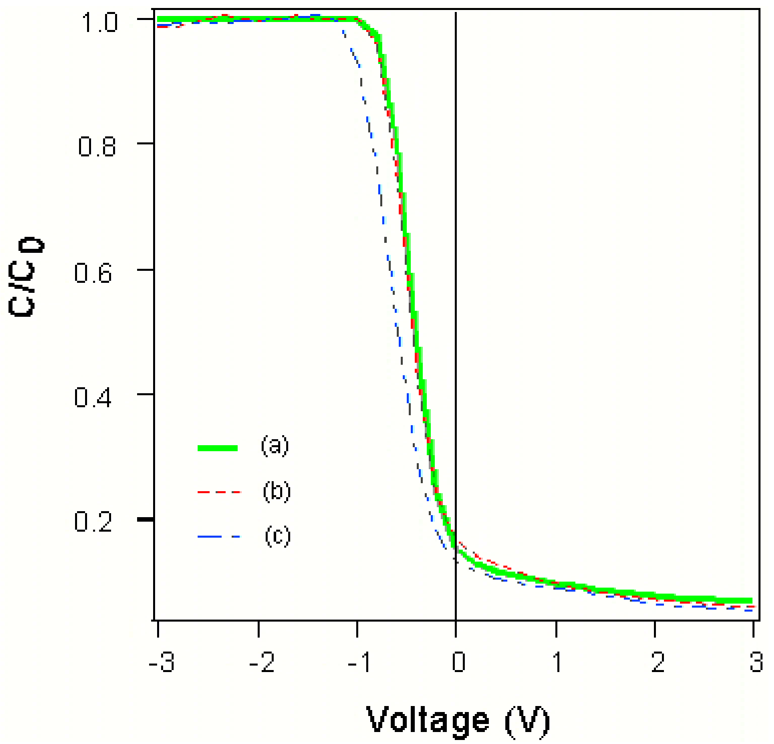

**Figure 5.6** C-V tests of Cu/Ru/$SiO_2$/Si capacitors with Ru film thicknesses of 4 nm and 2.5 nm before (a) and after annealing ((b) 4 nm Ru and (c) 2.5 nm Ru). The Ru films were annealed at 623 K for 60 minutes in $H_2$(10%)/$N_2$ ambient

Figure 5.7 shows C-V tests of (a) a composite 2.9 nm Ru/0.6 nm Ta film and (b) after 60 minutes annealing at 623 K in $H_2$ (10%)/$N_2$ ambient. There is negligible change of C-V curves after thermal annealing, which means this 3.5 nm composite Ru/Ta film effectively prevent Cu diffusion. Our electrical test results (not shown) also demonstrated that the 0.6 nm Ta film alone was not a good diffusion barrier. We don't know the mechanism why the composite Ru/Ta film is an effective barrier and further study is needed. One possible mechanism is that an amorphous Ru/Ta interfacial layer exists, which prevents Cu diffusion.

## 5.4 Summary

In summary, a pure and polycrystalline Ru film was grown on $SiO_2$ by thermal CVD using a $Ru_3(CO)_{12}$ precursor. The Ru/$SiO_2$ interface was thermally stable up to 673 K and the Scotch$^{TM}$ tape test demonstrated the good adhesion between each layer in the Cu/Ru/$SiO_2$ multilayer structure. The Ru film had a poor step coverage on a 600 nm wide $SiO_2$ trench with a 2:1 aspect ratio which may be attributed to the high reactive sticking coefficient of $Ru_3(CO)_{12}$. A 4 nm Ru film and a 2.9 nm Ru/0.6 nm Ta composite film are effective copper diffusion barriers under 60 minutes annealing at 623 K in $H_2$(10%)/$N_2$ ambient.

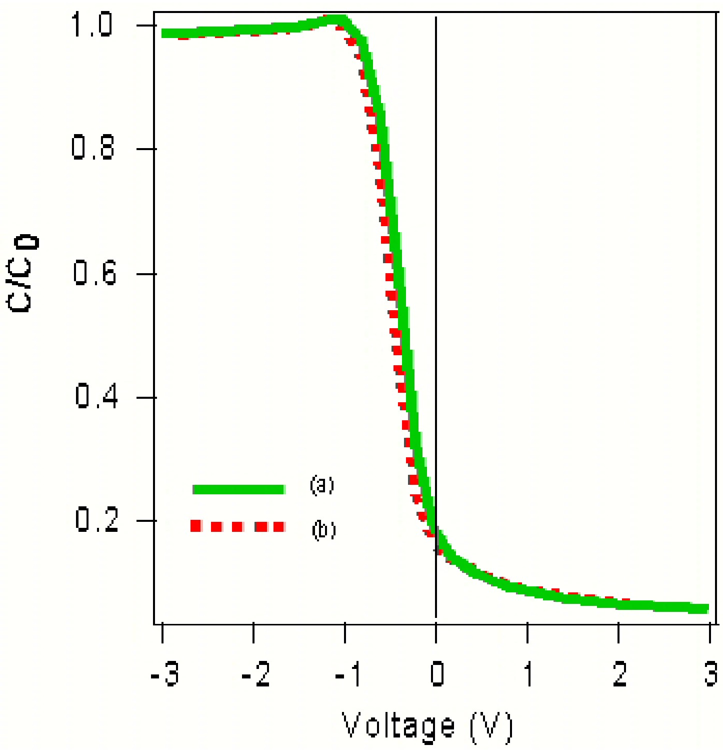

**Figure 5.7** C-V tests of (a) a composite 2.9 nm Ru/0.6 nm Ta film and (b) after 60 minutes annealing at 623 K in $H_2$ (10%)/$N_2$ ambient.

## 5.5 References

[1] J. Emsley, The Elements, 3rd ed. (Oxford, 1998)

[2] E.-S. Choi, J.-C. Lee, J.-S. Hwang, and S.-G. Yoo, Jpn. J. Appl. Phys. Part 1, **38**, 5317 (1999)

[3] S. K, Dey, J. Goswami, D. Gu, H. d. Waard, S. Marcus, and C. Werkhoven, App, Phys. Lett. **84**, 1606 (2004)

[4] O. J. Kwon, S. H. Cha, and J. J. Kim, J. Electrochem. Soc. 151, C127 (2004)

[5] Q. Wang, J. G. Ekerdt, D. Gay, Y.-M. Sun, and J. M. White, App. Phys. Lett. **84**, 1380 (2004)

[6] I. Goswami and R. Laxman, Semiconductor International, **27**, 49 (2004)

[7] Chyan, T. N. Arunagiri, and T. Ponnuswamy, J. Electrochem. Soc. **150**, C347 (2003)

[8] B. Massalski, Editor, Binary Alloy Phase Diagram, 2nd ed. (Materials Information Society, Material Park, OH, 1990).

[9] M. L. Green, M. E. Gross, L. E. Papa, K. J. Schnoes, and D. Brasen, J. Electrochem. Soc. **132**, 2677 (1985).

[10] C. J. Smart, A. Gulhati, and S. K. Reynolds, Mat. Res. Soc. Symp. Proc. **363**, 207 (1995)

[11] S. E. Park, H. M. Kim, K. B. Kim, and S. H. Min, J. Electrochem. Soc. **147**, 203 (2000)

[12] J.-H. Lee, J.-Y. Kim, S.-W. Rhee, D.-Y. Yang, D.-H. Kim, C.-H. Yang, Y.-K. Han, and C.-J. Hwang, J. Vac. Sci. Technol. A **18**, 2400 (2000).

[13] Y. Matsui, M. Hiratani, T. Nabatame, Y. Shimamoto, and S. Kimura, Electrochem. Solid-State Lett. **4**, C9 (2001).

[14] T. Nabatame, M. Hiratani, M. Kadoshima, Y. Shimamoto, Y. Matsui, Y. Ohji, I. Asano, T. Fujiwara and T.Suzuki, Jpn. J. Appl. Phys. Part2, **39**, L1188 (2000)

[15] T. Aoyama and K. Eguchi, Jpn. J. Appl. Phys. Part 2 **38**, L1134 (1999)

[16] M. Y. Kwak, D. H. Shin, T. W. Kang, and K. N. Kim, Thin Solid Films **339** 290 (1999)

[17] S. K. Rha, W. J. Lee, S. Y. Lee, Y. S. Hwang, Y. J. Lee, D. I. Kim, D. W. Kim, S. S. Chun, and C. O. Park, Thin Solid Films, **320**, 134 (1998)

[18] F. Braud, J. Torres, J. Palleau, J. L. Mermet, C. Marcadal, and E. Richard, Microelectronic Engng. **33**, 293 (1997)

[19] H. Kizil and C. Steinbruchel, Thin Solid Films, **449**, 158 (2004)

[20] H. Kizil, G. Kim, C. Steinbruchel, and B. Zhao, J. Electro. Mater. **30**, 345 (2001)

[21] A. A. Istratov, C. Flink, and E. R. Weber, Phys. Stat. Sol. (b) **222**, 261 (2000)

[22] Y.-M. Sun, S. Y. Lee, A. M. Lemonds, E. R. Engbrecht, S. Veldman, J. Lozano, J. M. White, J. G. Ekerdt, I. Emesh and K. Pfeifer, Thin Solid Films **397**, 109 (2001).

# Chapter 6 Summary

## 6.1 Conclusions

The cermet, Al/$Al_2O_3$ deposited on clean Si(1 0 0), was investigated for the mechanism of its transformation induced by laser irradiation. The films were deposited by reactive sputter deposition and, subsequently, irradiated with a single 1064 nm laser pulse in ambient air and $10^{-2}$ Torr vacuum. Characterization included X-ray photoelectron spectroscopy, scanning electron microscopy and atomic force microscopy. Irradiation in vacuum led to re-distribution of components within the first ~35 nm beneath the surface. Irradiation in air increased the concentration of $Al_2O_3$ in the same region. Irradiation increased the RMS surface roughness by a factor of 10 in both environments (from 3.5 to 36 nm). On the other hand, Al films irradiated in air do not oxidize measurably with a single laser pulse. Model calculations indicate that a single laser pulse (~16 MW $cm^{-2}$) can increase the local temperature of cermet from 300 to 1200 K. We interpret the observed transformations as a result of local heating and, in air, as accompanying thermal oxidation. With respect to using this material in thin film form as a resist for thermal patterning, we note a concern in that the observed thermal transformation requires very high transient temperature changes.

In order to achieve real-time surface analysis during thermal annealing, a continuous wave $CO_2$ infrared laser was coupled to a surface analysis system equipped for x-ray photoelectron spectroscopy (XPS) and ion scattering spectroscopy (ISS). The laser beam was directed into the vacuum chamber through a ZnSe window to the back side of the sample. With 10 W laser output, the sample temperature reached 563 K. The chamber remained below $10^{-8}$ Torr during annealing and allowed XPS and ISS data to be gathered as a function of time at selected temperatures. Compared with other heating methods, the high power density (up to 90 W/cm$^2$) and tight focus (0.28 cm$^2$) is a distinct advantage. Localization of the radiant energy makes it possible to minimize problems associated with species desorbing from non-sample surfaces and subsequently contaminating the surface of interest. Real time $Cu_2O$ reduction at 563 K was investigated.

Thermal chemical vapor deposition at temperatures as low as 423 K, using $Ru_3(CO)_{12}$ with no accompanying reactive gas, forms pure, uniform, and smooth Ru films on Ta and low resistivity films on $SiO_2$. Measured using XPS and ISS and assuming smooth films, a 2.5-nm-thick Ru film fully covers the underlying Ta, and the Ru film is thermally stable up to 573 K. A 6 nm Ru film can be an effective oxygen barrier to prevent underlying Ta from oxidation when subjected to conditions of either high vacuum annealing or exposure to ambient air. Unlike Ta, Ru films exhibit excellent wetting by Cu even when the Ru surface is contaminated with small amounts of oxygen.

Pure and polycrystalline Ru films were deposited on $SiO_2$ by the same thermal CVD process using $Ru_3(CO)_{12}$. The Ru film is thermally stable up to 673 K and has good adhesion properties with Cu and $SiO_2$, but the Ru film exhibits poor growth conformity on patterned $SiO_2$. A 4 nm Ru film and a 2.9 nm Ru/0.6 nm Ta composite film are effective copper diffusion barriers under 60 min annealing at 623 K in $H_2$(10%)/$N_2$ ambient.

## 6.2 Recommendations for future work

One of the important topics I address in this dissertation is to study Ru as a potential copper diffusion barrier material for ULSI interconnects. Recently, Ru has attracted much attention from the semiconductor industry, and many SRC and Sematech member companies have showed strong interests in our Ru project. Therefore, continuing to drive our current study forward is very necessary and exciting. In my past works, I have developed a low temperature chemical vapor deposition route to deposit thin Ru films on Ta and $SiO_2$, and completed several characterization works on material, physical, and electrical properties, thermal stabilities, adhesion properties, etc. The following issues may be addressed for further studies:

First of all, the ruthenium carbonyl ($Ru_3(CO)_{12}$) precursor we are using provides several unique benefits to the manufacturability of the Ru CVD process, such as simple and labile CO leaving groups, no co-dosing oxidizing gas, and low temperature deposition (150 $^{o}$C). However, this precursor has a very low deposition rate due to its low vapor pressure, and the precursor itself gradually decomposes inside the bubbler. Therefore it is noteworthy to consider developing a liquid injection delivery system to replace the current solid-state precursor delivery system so as to provide a reliable and high precursor flux rate for faster Ru film deposition.

Second, considering poor step coverage and polycrystalline film structure resulting from the current thermal CVD process, an atomic layer deposition (ALD) of Ru process is desired since it provides exact control of film thickness, amorphous film structure, and superb conformal growth in a high aspect-ratio trench and via holes. However, all of the reported Ru ALD processes in literature required the use of an oxidizing gas, for example, oxygen, to assist in cracking the Ru precursor compounds. Because this oxidizing gas will oxidize the underlying substrate, such as Cu or Ta, these ALD Ru process may not be applicable for the Cu interconnect process. Therefore, developing a new Ru precursor and an ALD route using reducing reactive gases such as hydrogen and ammonia, is highly desirable.

Finally, more studies should be addressed on the evaluation of Ru barrier properties. One important issue is what thickness is the minimum for a Ru film to be an effective copper diffusion barrier? Our electrical test results showed the 2.5 nm thick Ru film made by current CVD process could not effectively prevent Cu diffusion. ISS measurement results in chapter 4 and 5 showed our current thermal CVD process causes a 3-D island growth mode.

Because of Cu insolubility with Ru, the film microstructure is the major determining factor of barrier performance. Therefore, if we could develop an ALD Ru process in the future, the film would grow layer by layer, and an amorphous film structure may be obtained so that a thinner Ru film may work as an effective diffusion barrier. In addition, our electric tests also showed a composite Ru/Ta film could be an effective barrier, but we are not certain by which mechanism it operates. Interfacial chemistry between Ru and Ta should be investigated thoroughly.

In this dissertation, we combine XPS and ISS to measure Ru film continuity. This is a valuable and powerful method, and we have also extended its applications to studies on the film continuity of ALD $HfO_2$ films and monolayer identification of self-assembling organic molecule films. Compared with cross-sectional TEM measurement, this method is more convenient, time-saving, and allows *in-situ* measurement without breaking the vacuum. However, it is well to keep in mind that ISS has its own detection limit. When the target film is faitly rough, due to the shadow effect, the ISS substrate peak may disappear before the ad-layer fully covers the substrate. Moreover, it is very important to know that XPS measurement only provides an average film thickness. In some special conditions such as an extremely rough film surface, the film thickness calculated by XPS substrate peak attenuation may deviate away from the real film thickness. Dr. Yangming Sun and other White and Ekerdt group members are now combining SEM, EDS, AFM, TEM and

Quartz microbalance mass measurement to study how the film morphology, microstructure and uniformity affect the XPS thickness calculation results. We hope to work out general applicability conditions of XPS film thickness measurements. Also, for any new film growth process in the future, it may always be noteworthy to do cross-sectional TEM for a few selected samples to check with the accuracy of film thickness measured by XPS.

Lastly, I want to say some words about the *in-situ* laser annealing system we developed for real time surface analysis. Using this system, we can extend our surface chemistry study to any kind of sample, conducting, semi-conducting, and insulating, as long as the sample can absorb laser irradiation. Moreover, combining this real time surface analysis system with our film deposition and *in-situ* sample transfer systems, we can investigate in real time many of the film properties at elevated temperatures such as film agglomeration, inter-diffusion, thermal stability, surface and interfacial reaction, etc. In summary, this is a unique and very useful system, and wider application of this system for our future research is recommended.

# Bibliography

International Technology Roadmap for Semiconductors, 2001 Edition, http://public.itrs.net/, (2001).

C. Ahrens, R. Ferretti, G. Friese and J. O. Weidner, Microelectron. Eng. **37/38**, 211 (1997)

T. Aoyama and K. Eguchi, Jpn. J. Appl. Phys. Part 2 **38**, L1134 (1999)

E. P. Boyd, D. R. Ketchum, H. Deng, and S. G. Shore, Chem. Mater. **9**, 1154 (1997).

T. Brunner, IEDM, IEEE, 9 (1997)

D. Briggs and M. P. Seah, Practical surface analysis, 2nd ed., Vol. 1, 2 (Wiley, London, 1992).

D. Burgess, Jr., P. C. Stair, E. Weitz, J. Vac. Sci. Technol. A **4** 1362 (1986)

F. Braud, J. Torres, J. Palleau, J. L. Mermet and M. J. Mouche, Appl. Surf. Sci. **91**, 251 (1995)

F. Braud, J. Torres, J. Palleau, J. L. Mermet, C. Marcadal and E. Richard, Microelectron. Eng. **33**, 293 (1997)

J. Canning, Int. conference on microelectronic test structures, IEEE **11**, 25 (1998)

C. R.A. Catlow, et al., Mass transport in solids, Plenum Press, 1983

J. P. Chang, C. B. Case, H. W. Krautter, J. Sapjeta, R. L. Opila, and M. A. Decker, Proc. Electrochem. Soc. **99**, 261 (1999)

L. Chen, N. Magtoto, B. Ekstrom, and J. Kelber, Thin Solid Films **376**, 115 (2000).

E.-S. Choi, J.-C. Lee, J.-S. Hwang, and S.-G. Yoo, Jpn. J. Appl. Phys. Part 1, **38**, 5317 (1999)

J.-C. Chuang, S.-L. Tu and M.-C. Chen, J. Electrochem. Soc. **146**, 2643 (1999)

O. Chyan, T. N. Arunagiri, and T. Ponnuswamy, J. Electrochem. Soc. **150**, C347 (2003)

S. K, Dey, J. Goswami, D. Gu, H. d. Waard, S. Marcus, and C. Werkhoven, App, Phys. Lett. **84**, 1606 (2004)

D. J. Ehrlich, J. Y. Tsao, C.O. Bozler, J. Vac. Sci. Technol. B **3**, 1 (1985)

J. Emsley, The Elements, 3rd ed. (Oxford, 1998)

P.C. Fazan and M. Declercq, URSI International Symposium, IEEE 128 (1998)

J. Golden, C. Hawker, and P. Ho, Semiconductor International, **24**, 79 (2001)

I. Goswami and R. Laxman, Semiconductor International, **27**, 49 (2004)

M. L. Green, M. E. Gross, L. E. Papa, K. J. Schnoes, and D. Brasen, J. Electrochem. Soc. **132**, 2677 (1985).

R. H. Havemann and J. A. Hutchby, Proc. of IEEE **89**, 586 (2001)

Y. Z. Hu, R. Sharangpani and S.-P. Tay, J. Electrochem. Soc. **148**, G669 (2001).

A. Istratov, C. Flink and E. Weber, Phys. Stat. Sol. B, **222**, 261 (2000)

A. Istratov and E. Weber, J. Electrochem. Soc. **149**, G21 (2002)

C. Jezewski, W. A. Lanford, C. J. Wiegand, J. J. Senkevich, T. Lu, Semiconductor International, **27**, 56 (2004)

A. Kaloyeros, C.Xiaomeng, T. Stark, K. Kumar, S. Soon-Cheon, G. Peterson, H. Frisch, B. Arkles and J. Sullivan, J. Electrochem. Soc. **146**, 170 (1999)

H. Kizil, G. Kim, C. Steinbruchel and B. Zhao, J. Electron. Mat. **30**, 345 (2001)

A. Kohn, M. Eizenberg, Y. Shacham-Diamand, B. Israel, Y. Sverdlov, Microelectron. Eng. **55**, 297 (2001)

R. Koger, M. Eizenberg, D. Cong, N. Yoshida, L. Chen, S. Ramaswami, D. Carl, Microeletron. Eng. **50**, 375 (2000)

M. Kwak, D. Shin, T. Kang and K. Kim, Thin Solid Films **339,** 290 (1999)

M. Kwak, D. Shin, T. Kang and K. Kim, J. Appl. Phys. **38**, 5792 (1999)

M. Y. Kwak, D. H. Shin, T. W. Kang and K. N. Kim Phys. Stat. Sol. (a) **174**, R5 (1999)

O. J. Kwon, S. H. Cha, and J. J. Kim, J. Electrochem. Soc. 151, C127 (2004)

T. Laurila, K. Zeng, J. K. Kivilahti, J. Molarius, and I. Suni, J. Appl. Phys. **88**, 3377 (2000)

C. S. Lee, H. Gong, R. Liu, A. T. S. Wee, C. L. Cha, A. See, and L. Chan, J. of Appl. Phys. **90**, 3822 (2001)

J.-H. Lee, J.-Y. Kim, S.-W. Rhee, D.-Y. Yang, D.-H. Kim, C.-H. Yang, Y.-K. Han, and C.-J. Hwang, J. Vac. Sci. Technol. A **18**, 2400 (2000).

Y. K. Lee, M L. Khin, J. Kim, K. Lee, Mat. Sci. Semicond. Processing, **3**, 179 (2000)

S.Y. Lee, N. Mettlach, N. Nguyen, Y.-M. Sun and J.M. White, Appl. Surf. Sci. (submitted) (2002).

A. M. Lemonds, Ph. D Dissertation, The University of Texas at Austin, (2003)

David. R. Lide, et al., Handbook of chemistry and physics, 78th edition (1997)

L. Liu, H. Gong, Y. Wang, A. Wee, R. Liu, Int. J. Modern Phys. B **16**, 322 (2002)

K. Maex, M. R. Baklanov, D. Shamiryan, F. Lacopi, S. H. Brongersma, and Z. S. Yanovitskaya, J. Appl. Phys., **93**, 8793, (2003)

B. Massalski, Editor, Binary Alloy Phase Diagram, 2nd ed. (Materials Information Society, Material Park, OH, 1990).

Y. Matsui, M. Hiratani, T. Nabatame, Y. Shimamoto, and S. Kimura, Electrochem. Solid-State Lett. **4**, C9 (2001)

M. Matsui, T. Tatsumi and M. Sekine, J. Vac. Sci. Technol. A **19**, 1 (2001)

J. Melngailis, A. A. Mondelli, I. L. Berry, R. Mohondro, J. Vac. Sci. Technol. B **16**, 927 (1998).

J. Melngailis, D. J. Ehrlich, S. W. Pang, and J. N. Randall, J. Vac. Sci. Technol. B **5**, 379 (1987)

K.-H. Min, K.-C. Chun, and K.-B. Kim, J. Vac. Sci. Technol. B **14**, 3263 (1996)

T. Nabatame, M. Hiratani, M. Kadoshima, Y. Shimamoto, Y. Matsui, Y. Ohji, I. Asano, T. Fujiwara and T.Suzuki, Jpn. J. Appl. Phys. Part2, **39**, L1188 (2000)

S. Nonogaki, T. Ueno, and T. Ito, Microlithography: Fundamentals in Semiconductor Devices and Fabrication Technology (New York Marcel Dekker, Inc., New York, NJ, 1998)

T. Oku, E. Kawakami, M. Uekubo, K. Takahiro, S. Yamaguchi, and M. Murkami, Appl. Surf. Sci. **99**,265 (1996)

S. W. Pang, R. R. Kunz, et al., J. Vac. Sci. Technol. B **7** 1624 (1989)

S. E. Park, H. M. Kim, K. B. Kim, and S. H. Min, J. Electrochem. Soc. **147**, 203 (2000)

L. Peters, Semiconductor International, **24**, 66 (2001)

L. Peters, Semiconductor International, **25**, 55 (2002)

M. P. Petkov, Low-k interlevel dielectrics technology, http://nepp.nasa.gov/index_nasa.cfm/810/

J. D. Plummer, M. D. Deal, and P. B. Griffin, Silicon VLSI Technology Fundamentals, Practice and Modeling (Prentice Hall, Upper Saddle River, NJ, 2000).

S. Poulston, P. M. Parlett, P. Stone and M. Bowker, Surf. Interface Anal., **24** 811 (1996)

M. Pourbaix, Atlas of Electrochemical Equilibria in Aqueous Solutions, 1st ed. (Oxford, 1966)

G. Pugh, J. Canning, and B. Roman, IEEE custom integrated circuits conference, 149 (1998)

W. Qin, Z. Q. Mo, L. J. Tang, B. Yu, S. R. Wang, and J. Xie, J. Vac. Sci. Technol. B **19**, 1942 (2001)

S. K. Rha, W. J. Lee, S. Y. Lee, Y. S. Hwang, Y. J. Lee, D. I. Kim, D. W. Kim, S. S. Chun and C. O. Park, Thin Solid Films **320**, 134 (1998)

G. V. Samsonov, The oxide handbook (IFI/Plenum Press, 1973)

Y. Shacham-Diamand, J. Electro. Mat. **30**, 336 (2001)

P. Singer, Semiconductor International, **25**, 46 (2002)

C. J. Smart, A. Gulhati, and S. K. Reynolds, Mat. Res. Soc. Symp. Proc. **363**, 207 (1995)

James E. Stewart, Optical principles and technology for engineers (Marcel Dekker Inc., 1996)

Y.-M. Sun, S. Y. Lee, A. Lemonds, J. Lozano, J.-P. Zhou, J. G. Ekerdt, J. M. White, I. Imesh, Surf. Interface Anal. **32**, 79 (2001)

Y.-M. Sun, S. Y. Lee, E. R. Engbrecht, K. Pfeifer, S. Smith, J. M. White and J. G. Ekerdt, Mater. Res. Soc. Symp. Proc. **648,** P6.43 (2001)

Y.-M. Sun, S. Y. Lee, A. M. Lemonds, E. R. Engbrecht, S. Veldman, J. Lozano, J. M. White, J. G. Ekerdt, I. Emesh and K. Pfeifer, Thin Solid Films **397**, 109 (2001)

W. H. Teh, L. T. Koh, S. M. Chen, J. Xie, C. Y. Li, P. D. Foo, Electron. Lett. **37**, 660 (2001)

William J. Tropf, et al., Handbook of optical constants of solid (Academic Press, 1998)

M. Wang, L. Chen and M. Chen, J. Electrochem. Soc. **146**, 728 (1999)

Q. Wang, J. G. Ekerdt, D. Gay, Y.-M. Sun, and J. M. White, App. Phys. Lett. **84**, 1380 (2004)

S. Wang, MRS bull. **19**, 30 (1994)

S. Wang, H. Tsai, S. Sun, J. Appl. Phys. **40**, 2642 (2001)

C. Whitman, M. M. Moslehi, A. Paranjpe, L. Velo, and T. Omstead, J. Vac. Sci. Technol. A **17** 1893 (1999)

J. I. B. Wilson, J. S. Walton and G. Beamson, J. Electron Spectrosc. Relat. Phenom., **121**, 183 (2001)

S. Wolf, Silicon Processing for the VLSI Era, Vol. 4 Deep-Submicron Process Technology (Lattice Press, Sunset Beach, CA, 2002)

# Vita

Qi Wang was born in Beijing, P. R. China on April 21, 1973, the son of Zhaozheng Wang and Xiaoying He. Qi earned his Bachelor of Engineering in Chemical Engineering from Tsinghua University, China in July 1996, graduating with the highest honor. He won the Yi-Er-Jiu outstanding student scholarship and other excellent student scholarships during his undergraduate study. He conducted undergraduate research in the group of Professor Fuxin Ding, studying kinetics and mass transfer phenomena of gas-liquid loop reactors. In September 1996, he was admitted to the graduate school of Tsinghua University, waiving the admission tests, and conducted his research under the supervision of Professor Fuxin Ding and Naiju Yuan studying the kinetics of waste-water treatment of the activate sludge in a column reactor. He was awarded an excellent graduate student scholarship in 1998. Qi earned his Master of Science in Chemical Engineering in July 1999.

Qi came to Austin, TX in August 1999 and started his Ph. D program study at in the Department of Chemical Engineering at the University of Texas at Austin under the guidance of Dr. John Michael White. Qi's research addressed the thin film deposition and surface chemistry for developing new materials and technologies for next generations of semiconductor manufacturing process. His research projects included Al/$Al_2O_3$ thin film growth and its laser transformation, *in-situ* laser annealing system for real time surface kinetics analysis, electron beam induced etching and deposition of heavy metals for sub-100 nm photomask repair and fabrication, and low temperature chemical vapor deposition (CVD) and characterization of ruthenium thin films as potential copper diffusion barriers for ULSI copper interconnect. Parts of Qi's research had already attracted strong interests from the semiconductor industry, and also brought him to win an internship at Novellus Systems Inc. in San Jose, CA during the summer of 2003. In the research and development department, he worked on the deposition and characterization of CVD thin films for future technology nodes of integrated circuit fabrication.

Qi has authored and coauthored eleven publications in peer-reviewed journals. Research results were presented at the Texas Surface Science Round-up annual meeting in Winedale, TX in May 2001; the 58th Southwest Regional Meeting of American Chemical Society in Austin, TX in August 2002; SRC-CAIST Annual Review meeting in Albany, NY in Oct. 2003, the 50th American Vacuum Society International Symposium in Baltimore, MI in Nov. 2003; and SRC/DAPRA Annual Review meeting in Madison, WI in July, 2004.

Permanent address: 1634 West 6th street Apt P Austin, TX 78703

This dissertation was typed by the author.